Limited influence of bedrock strength on river profiles: the dominant role of sediment dynamics

Nanako Yamanishi[1] and Hajime Naruse[1]

[1]Division of Earth and Planetary Science, Graduate School of Science, Kyoto University, JP

Correspondence: Nanako Yamanishi (yamanishi.nanako.23r@gmail.com)

Abstract. Bedrock river incision is a fundamental process driving the evolution of mountainous landscapes. Bedrock strength is often considered a primary control on incision rates and river profile morphology, with laboratory experiments showing a strong correlation between erosion rate and tensile strength. However, in natural settings, lithological boundaries frequently do not correspond to changes in the channel gradient. This study addresses this apparent paradox by integrating field observations with numerical experiments in the tributaries of the Abukuma River basin, northeastern Japan. Field surveys were conducted to measure bedrock tensile strength, riverbed gravel grain size, and the spatial distribution of lithologies. Despite more than an order-of-magnitude variation in bedrock tensile strength across the study area, the channel slopes remained nearly uniform. Numerical experiments were performed using three models of bedrock river erosion to investigate the underlying mechanisms. Among them, the sediment-flux-dependent model, which explicitly incorporates sediment cover and tool effects, most accurately reproduced the observed longitudinal profiles. The results reveal that the local lithology does not directly influence channel slope due to a negative feedback between sediment cover and river gradient. Increased erodibility reduces slope, which enhances sediment coverand Higher bedrock erodibility reduces channel slope and sediment transport capacity, promoting sediment cover. The resulting sediment cover suppresses further erosion , thereby offsetting the impact and offsets the effect of bedrock strength. These findings highlight the limited role of bedrock strength in controlling channel gradients and underscore the importance of sediment dynamics, particularly sediment supply and grain size, in shaping fluvial topography. Future research should explore how lithology-dependent variations in sediment characteristics influence river profile development.

1 Introduction

Bedrock river incision driven by fluvial processes plays a fundamental role in shaping mountainous landscapes (Whipple, 2004; Howard, 1994). This incision results froma combination of processes, including weathering, : abrasion by saltating particles produced by weathering on hillslope, plucking, cavitation, and debris scouring (Whipple et al., 2013; Campforts et al., 2020). While channel slope and drainage area have long been recognized as key controls of river incision, recent studies emphasize the importance of additional factors such as bedrock lithology, sediment grain size, and sediment supply (Sklar and Dietrich, 2001, 2004). Given the complexity of these controlsThese erosional processes are recorded in river longitudinal profiles; therefore, researchers have increasingly turned to river used river longitudinal profiles to reconstruct signals of past climate change and crustal uplift (e.g., Molnar and England, 1990; Pritchard et al., 2009).

Among the various controls on river incision, bedrock strength has often been assumed to exert a strong influence on erosion rates. Laboratory experiments have shown that incision rate can scale with the square of tensile strength (Sklar and Dietrich, 2001)of bedrock (Sklar and Dietrich, 2001; Inoue et al., 2017; Turowski et al., 2023), and recent field-based studies have highlighted its role in landscape evolution (Takahashi, 2025; Haag et al., 2025; Cruz Nunes et al., 2015; Korup and Schlunegger, 2009; Kühni and Pfiffner, 2001). For example, Haag et al. (2025) demonstrated a strong correlation between rock strength, erosion rate, and topography steepness in southeastern Brazil. These results suggest that the mechanical propertiesof bedrock should be a critical control

In hillslope regions, several studies have demonstrated that bedrock properties, including rock strength and structural orientation, exert primary controls on erosion rates, dominant processes, and mountain topography (Cruz Nunes et al., 2015; Korup and Schlunegger, 2009; Kühni and Pfiffner, 2001). For example, in the Alpine region, Korup and Schlunegger (2009) exhibited that catchment erosion rates in harder crystalline rocks are approximately $\sim$0.7 mm yr^{-1}, whereas rates in weaker lithologies such as schist and flysch reach $\sim$4 mm yr^{-1}. In addition, average hillslope gradients differ by up to 0.08 between gneiss and softer rocks (Korup and Schlunegger, 2009). These studies primarily focus on hillslope regions (slopes of $\sim$10–60%), where gravitational mass transport and weathering dominate sediment production and transport.

However, the effects of bedrock properties on river incision .

However, and channel morphology in alluvial-bedrock regions remain less well quantified. Some empirical observations of actual river longitudinal profiles often contradict this expectation. Even alluvial-bedrock rivers report that even in regions where the bedrock tensile strength varies by more than an order of magnitude, the local channel gradients remain remarkably uniform often remain uniform (Hayakawa and Oguchi, 2009; Takahashi, 2025). In theory, under steady-state conditions where erosion balances uplift, lower bedrock erodibility should result in steeper slopes to maintain the incision. Conversely, studies such as Hayakawa and Oguchi (2009) report that variations in bedrock strength do not necessarily coincide with changes in the channel gradient, challenging the predictive power of rock strength alone.

One explanation for this paradox is the sediment cover effect, which may play a more dominant role than rock hardness in regulating bedrock incision (Sklar and Dietrich, 2004; Sklar and Dietrich, 2006). Bedrock rivers commonly erode via the sediment tool effect, where moving clasts (Sklar and Dietrich, 2004; Sklar and Dietrich, 2006; Turowski et al., 2007).

Gilbert (1877) was the first to propose that the amount of transport sediment has two opposite effects on bedrock erosion, the tool effect and cover effect. River bedrocks are commonly eroded by moving clasts that abrade the channel bed (tool effect). However, this process is only effective when the sediment supply is sufficient to provide tools but not so abundant that the bed becomes completely covered. When cover becomes the cover is extensive, it shields the bedrock surface from direct impacts, thereby suppressing erosion rates (the cover effect). Guryan et al. (2024) demonstrated that models incorporating sediment cover yield more accurate predictions of river profiles, emphasizing the need to account for sediment dynamics.

Despite the growing recognition of the significance of the sediment cover effect, field-based quantification remains challenging. Molnar (2001) argued that the initiation of bedrock incision requires stream power to exceed a critical value necessary for gravel-cover entrainment. And its threshold value depends on the grain size (Sklar and Dietrich, 2004).

Although there are several attempts in the field measurements on to measure the sediment cover rate ratio under fair-weather conditions (Johnson et al., 2009; Carr et al., 2023), observations typically capture conditions during low flow. In contrast, most bedrock incisions Most bedrock incision episodes occur during rare, high-energy floods (Molnar, 2001); thus, the measured sediment cover under fair-weather conditions may not represent that during active erosion. Indeed, experimental studies by Fernández et al. (2019) indicated that transient, fluctuating sediment cover—rather than mean cover—governs the erosion potential, especially near the transitions between exposed and covered bedrock. Such temporal dynamics are difficult to capture through field snapshots alone.

Therefore, numerical modeling is essential for evaluating the spatial and temporal variability of the sediment cover and its geomorphic consequences (Sklar and Dietrich, 2006; Beer et al., 2017) because temporal dynamics are difficult to capture through field snapshots alone. Despite this understanding, relatively few studies have quantitatively examined the combined influence of bedrock strength and sediment cover on actual river profiles using direct measurements of rock strength (Turowski et al., 2023; Inoue et al., 2017).

This study aims to fill this gap by conducting systematic measurements of the bedrock tensile strength and grain size data in multiple tributaries of a bedrock river system and by using these data to inform the numerical models. We evaluated three numerical models that represent varying levels of complexity in their treatment of erosion processes: the sediment-flux-dependent model (SFDM) (Sklar and Dietrich, 2004; Sklar and Dietrich, 2006; Chatanantavet and Parker, 2009), the area-based stream power model (ASPM)(Howard, 1994; Campforts et al., 2020), and the stream power model with alluvium conservation and entrainment (SPACEM)(Shobe et al., 2017; Guryan et al., 2024). Among these, only SFDM explicitly accounts for the sediment tool effect, while ASPM considers only the bedrock strength. SPACEM incorporates both the bedrock strength and the sediment cover, but not the tool effect explicitly . (Shobe et al., 2017; Guryan et al., 2024).

By applying these models to field data, including measurements of grain size and bedrock strength, we conducted simulations to assess how well each model reproduces the observed river topographythey capture the actual responses of bedrock rivers to variations in bedrock strength. Our goal is to clarify how the relationship between the bedrock strength and the channel slope changes with or without the sediment cover effect, and which physical parameters are most essential for accurately capturing the longitudinal profile of bedrock rivers.

2 Geologic and Topographic settings

This study We investigated the tributaries of the Abukuma River near the Koriyama City in Fukushima, Japan (Fig. 1 (a)) , because in this region, studies on uplift and erosion rates have been extensively conducted (e.g. Tanaka et al., 1996; Fukuda et al., 2020; Matsushi et al., 2014). The Abukuma River drains the Nakadori area in Fukushima, covering draining an area of 5,400 km^2 and being 239 km in length. The study area is about 150 km from the river mouth, located in the west of the Koriyama City. Five tributaries, Takinosawa, Hisawa, Fukazawa, Sangasawa, and Gohyaku River, were surveyed. Four of these tributaries (Takinosawa, Hisawa, Fukazawa, and Sangasawa) join the Gohyaku River, which merges into the mainstream of the Abukuma River (Fig. 1 (c), Tab. 1). These rivers are all bedrock rivers where the channel floor is partially covered with gravel.

The study area is in the forearc region of the Northeastern Japan Arc, which is bounded by the Tanakura tectonic line from the Southwestern Japan Arc (Ichikawa, 1990). A gentle synclinal structure with an NNE-SSW trending fold axis exists in this area, where the strata dip $<$ 20°–40°in the maximum. Several North-South trending faults are distributed in this study , while they are not active faults (Kubo et al., 2003; Yamamoto and Sakaguchi, 2023)region, although they are inactive faults (Kubo et al., 2003; Yamamoto and Sakaguchi, 2023).

The bedrock of the study area is composed of metamorphic rocks, the Cretaceous igneous rocks, the Middle Miocene sedimentary rocks, and the Late Miocene pyroclastics with Late Miocene pyroclastic and volcanic rocks. The metamorphic rocks are the composed of muscovite-biotite-plagioclase-quartz gneiss, distributed in the central region of the study area. Their formative Formation age is unknown. The Lower Cretaceous Abukuma granitic rocks, consisting of the granodiorite (Kubo et al., 2003) in the surveyed area, are distributed in the northern region of the study area. The Middle Miocene Horiguchi Formation, consisting of marine sedimentary rocks, is distributed in the southwestern region of the study area (Yamamoto and Sakaguchi, 2023). Massive sandstones and alternating beds of parallel-laminated sandstones and siltstones occur in this formation. The Late Miocene Kogyoku Formation is composed mainly of pyroclastic flow deposits filling the Kogyoku Caldera. They are distributed in the northeastern region of the study area (Yamamoto and Sakaguchi, 2023). Dacite, lapilli tuff, and tuff breccia occur in the Formationformation. In addition to these formationsunits, intrusive dacites and andesites occur in both igneous and sedimentary sequences.

The upliftVarious studies implied that the rock uplift, exhumation, and denudation rates of the drainage basin of the Abukuma River were quantified using various methods. From the coastal and river terrace surfaces formed along the mainstreamAbukuma River drainage basin are lower than those of adjacent regions. Based on geomorphic analyses, Fujiwara et al. (2005) estimated the average rock uplift rate of this basin as the Abukuma basin to be 0–0.3 m mm yr^{-1} (Fujiwara et al., 2004) for the recent over the past 100 ,000 years. Apatite kyr. This estimate was derived from the relative heights of fluvial terrace surfaces formed during the Last Interglacial and the preceding glacial period (Tanaka et al., 1996; Yoshiyama and Yanagida, 1995), combined with interpolation of uplift rates from surrounding areas (Fujiwara et al., 2004). Longer-term exhumation rates of this region were constrained using apatite and zircon (U-Th)/He thermochronometryalso suggested the denudation rates of this region. Fukuda et al. (2020) applied . Applying this method to the Cretaceous granitic rocks in the Abukuma mountain area, estimating that it is about 0.01 Mountains, Fukuda et al. (2020) estimated Myr-scale exhumation rates of approximately 0.02–0.03 mm yr^{-1}.

The erosion rate was also estimated using terrestrial cosmogenic nuclides formed near the bedrock surface. Matsushi et al. (2014) measured denudation rates in the Abukuma Mountains using terrestrial cosmogenic nuclides and concluded that the denudation rate is In addition, terrestrial cosmogenic nuclide analyses indicated denudation rates of 0.076–0.124 mm yr^{-1} . In summary, most of the results agreed that the denudation rates of the drainage basin of the Abukuma River are relatively slow (less than 0.3 mm yr^{-1}), compared with the denudation rates ranging from for the Abukuma River drainage basin (Matsushi et al., 2014).

In contrast, the Ou Backbone Range, which forms the tectonic core of the northeastern Japan Arc, exhibits substantially higher exhumation rates of approximately 0.1to 1 –1.5 mm yr^{-1} in the Ou Backbone Range, the central region of the Northeastern Japan Arc (Fukuda et al., 2020)(Fukuda et al., 2020). These values are roughly an order of magnitude greater than those estimated for the

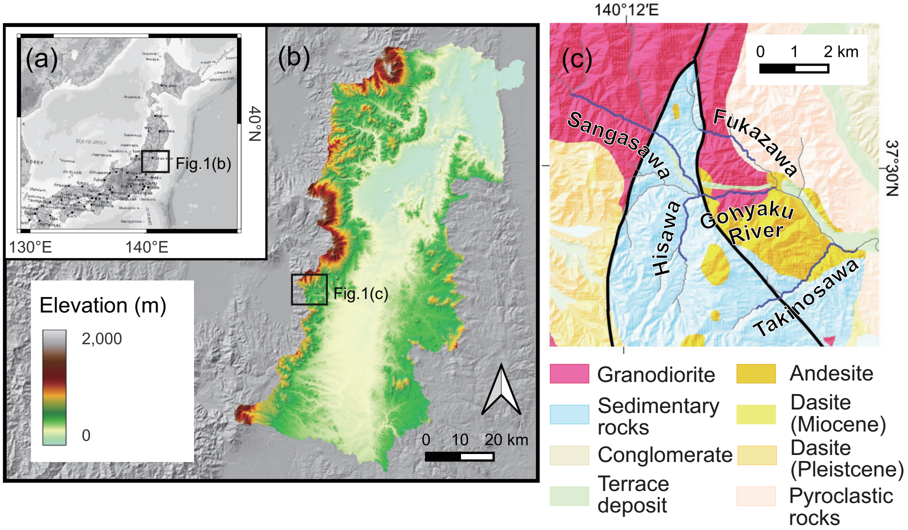

Figure 1. Index map and surveyed areas. The map data were obtained from the Technical Report of the Geospatial Information Authority of Japan. (a) Location of the Abukuma River basin. (b) Map of the Abukuma basin. The topographic elevation is exhibited in colors. (c) Geological map with surveyed tributaries. Black lines indicate major faults, and blue lines indicate the researched tributaries.

Table 1. Tributary information. Takinosawa, Hisawa, Fukazawa, and Sangasawa are tributaries of Gohyaku River.

Name	Length (km)	Drainage Area (km^2)
Takinosawa	5.2	7.4
Hisawa	5.3	8.9
Fukazawa	8.4	13.7
Sangasawa	5.6	17.5
Gohyaku River	25.9	190

Abukuma River basin. Collectively, these studies demonstrate that the Abukuma River basin has experienced relatively low uplift and erosion rates compared with adjacent mountainous regions.

3 River incision model

Numerous bedrock incision models have been proposed not only to understand the formative mechanisms of the resulting in the formation of bedrock river profiles (e.g. , Sklar and Dietrich, 1998; Whipple and Tucker, 1999; Sklar and Dietrich, 2004; Inoue et al., 2014; Aubert et al., 2016) (e.g., Sklar and Dietrich, 1998; Whipple and Tucker, 1999; Sklar and Dietrich, 2004; Inoue et al., 2014; Aubert et al., 2016) but also to estimate the crustal uplift rates of mountainous regions (e.g. , Howard, 1994; Pritchard et al., 2009; Roberts et al., 2012)(e.g., Howard, 1994; Pritchard et al., 2009; Roberts et al., 2012). In those models, the following formulation was utilized to represent bedrock river elevation change in the continuous uplifting area area experiencing continuous rock uplift:

$$\frac{\partial \eta}{\partial t} = U - E \tag{1}$$

where η denotes bedrock surface elevation, U and E are the rock uplift and bedrock erosion rates, respectively. In the At steady state, the left side of Eq. (1) equals zero, and thus the erosion rate balances with the uplift rate. rock uplift is balanced by surface erosion.

Among various incision models (e.g., Howard and Kerby, 1983; Seidl and Dietrich, 1992; Tucker and Slingerland, 1994; Sklar and Dietrich, 2004; Lamb et al., 2008; Shobe et al., 2017), this study examined the sediment-flux-dependent model (SFDM) and two types of stream power models (Sklar and Dietrich, 2004; Chatanantavet and Parker, 2009; Inoue et al., 2017; Campforts et al., 2020; Guryan et al., 2024) to evaluate their appropriateness to account for assess how well they capture the actual responses of the bedrock rivers to differences variations in bedrock strength. SFDM (Sklar and Dietrich, 2004; Whipple and Tucker, 2002) focuses on the In SFDM (Sklar and Dietrich, 2004; Whipple and Tucker, 2002), abrasion-saltation process processes are explicitly represented as the dominant mechanism of bedrock incision (Sklar and Dietrich, 2004). This model considers that the flux of the impact kinetic energy of transported sediment particles determines the incision rate. The stream power models consider that the bedrock incision rates are proportional to the loss of the stream energy per unit time and area (i.e., stream power) (Howard, 1994). The formulations of these models are described in detail below.

3.1 Sediment-flux-dependent model

In the sediment-flux-dependent model (Sklar and Dietrich, 2004), the incision rate E [m s^{-1}] is obtained by:

$$E = V_i I_{r\mathrm{r}}(1 - P_{c\mathrm{c}}) \tag{2}$$

in which V_i is the average volume of bedrock detached per particle impact, I_r I_r is the rate of particle impacts per unit area per unit time, and P_c P_c is the fraction of the covered riverbed.

Regarding the bedrock as Assuming the bedrock to be an elastic brittle material, V_i can be rewritten by the classic impact wear model of Bitter (1963) as:

$$V_i = \frac{1/2M_p(U_i \sin\alpha)^2}{\varepsilon_v}\frac{1/2\mathsf{M}_\mathrm{p}(\mathsf{U}_\mathrm{i}\sin\alpha)^2}{\varepsilon_\mathrm{v}} \tag{3}$$

where M_p M_p [kg] denotes particle mass. U_i [m s^{-1}] indicates particle impact velocity the impact velocity of the particle, and α is saltation impact the saltation angle. The parameter ε_v ε_v [J] denotes the total energy required to erode a unit volume of rock (Sklar and Dietrich, 2004). The threshold energy ε_v ε_v is calculated by (Engle, 1978; Sklar and Dietrich, 2001):

$$\varepsilon_{v\mathrm{v}} = \frac{k_v\sigma_t^2}{2Y}\frac{\mathsf{k}_\mathrm{v}\sigma_\mathrm{t}^2}{2\mathsf{Y}} \tag{4}$$

where σ_t σ_t [MPa] is bedrock tensile strength, and k_v k_v denotes rock resistance coefficient. Y [MPa] represents Young's modulus. By substituting Eq. (4) into Eq. (3), we obtain:

$$V_i = \frac{\pi\rho_s D_s^3 w_{si}^2 Y}{6k_v\sigma_t^2}\frac{\pi\rho_\mathrm{s}\mathsf{D}_\mathsf{s}^3\mathsf{w}_\mathsf{si}^2\mathsf{Y}}{6\mathsf{k}_\mathrm{v}\sigma_\mathrm{t}^2} \tag{5}$$

where ρ_s ρ_s [kg m^{-3}] and D_s D_s [m] denote the density of sediment and the diameter of a spherical sediment grain, respectively. $M_p=\rho_s \pi D_s^3/6$ $M_\mathrm{p}=\rho_\mathrm{s}\pi D_\mathrm{s}^3/6$ is the mass of a spherical grain, and w_{si} [m s^{-1}] is the vertical component of the particle velocity on impact (i.e., $w_{si}=U_i \sin\alpha$).

Here, the number of particle impacts per unit time and area I_r I_r is proportional to the flux of the bedload particles and inversely proportional to the downstream distance between the impacts. Using the sediment flux volume per unit width q_s q_s [m^2 s^{-1}] and the saltation hop length L_s L_s [m], I_r I_r is expressed as:

$$I_{r\mathrm{r}} = \frac{\rho_s q_s}{M_p L_s} = \frac{6}{\pi D_s^3} q_s \frac{1}{L_s} \frac{\rho_\mathrm{s}\mathrm{q_s}}{\mathrm{M_p L_s}}. \tag{6}$$

Substituting $M_\mathrm{p}=\rho_\mathrm{s}\pi D_\mathrm{s}^3/6$ into Eq. (6),

$$\mathrm{I_r} = \frac{6}{\pi \mathrm{D_s^3}} \mathrm{q_s} \frac{1}{\mathrm{L_s}}. \tag{7}$$

Substituting Eqs. (5) and (7) into Eq. (2), bedrock incision rate E is recast as:

$$E = \frac{\rho_s w_{si}^2 Y}{L_s k_v \sigma_t^2} \frac{\rho_\mathrm{s} \mathrm{w_{si}^2 Y}}{\mathrm{L_s k_v} \sigma_\mathrm{t}^2} q_{s\mathrm{s}}(1-P_{c\mathrm{c}}). \tag{8}$$

Chatanantavet and Parker (2009) proposed that the abrasion coefficient can be defined as:

$$\beta = \frac{\rho_s w_{si}^2 Y}{L_s k_v \sigma_t^2} \frac{\rho_\mathrm{s} \mathrm{w_{si}^2 Y}}{\mathrm{L_s k_v} \sigma_\mathrm{t}^2}. \tag{9}$$

Using this formulation, Eq. (8) can be rewritten as:

$$E = \beta q_{s\mathrm{s}}(1-P_{c\mathrm{c}}). \tag{10}$$

Based on the flume experiments in the field scale, Inoue et al. (2014, 2017) pointed out that the erosion rate is proportional to the square root of the grain size rather than the shear stress and that it does not significantly depend on the Young's modulus. From this experimental result, Inoue et al. (2017) proposed the following relation:

$$E = \beta_0 \sigma_{t\mathrm{t}}{}^2 \left(\frac{D_s}{k_s} \frac{\mathrm{D_s}}{\mathrm{k_s}} \right)^{0.5} q_{s\mathrm{s}}(1-P_{c\mathrm{c}}) \tag{11}$$

where β_0 is an empirical coefficient (0.0001) [kg^{2}m^{-3}s^{-4}], k_s k_s [m] represents the hydraulic roughness heightheight of the hydraulic roughness, which is determined by the equation $k_s=\kappa_a P_c+\kappa_b(1-P_c)$$k_\mathrm{s}=\kappa_\mathrm{a} P_\mathrm{c}+\kappa_\mathrm{b}(1-P_\mathrm{c})$. Here, κ_a κ_a is a roughness coefficient that is linear to the grain diameter D_s, and κ_b D_s, and κ_b is a constant representing the bedrock roughness. We adopted this relation In Inoue et al. (2014), $\kappa_\mathrm{a}=2.5D_s$ and $\kappa_\mathrm{b}=0.0032$. We adopted these relations and values in the model calculation.

The bedrock covered ratio P_c P_c can be expressed in various ways; however, in this study, it is defined as:

$$P_{c\mathrm{c}} = \frac{q_s}{q_t} \frac{\mathrm{q_s}}{\mathrm{q_t}} \tag{12}$$

following the work of Sklar and Dietrich (2004). The sediment transport capacity q_t q_t [m^2 s^{-1}] takes the form (Luque and and, 1976): (E. Meyer-Peter, 1948; Luque and and, 1976):

$$q_{t\mathrm{t}} = 5.7(R_{b\mathrm{b}} g D_{s\mathrm{s}}{}^3)^{1/2}(\tau^* - \tau_{c\mathrm{c}}{}^*)^{\frac{3}{2}} \tag{13}$$

R_b where R_b denotes the nondimensional buoyant density of the sediment ($R_b = (\rho_s - \rho_w)/\rho_w$ $R_\mathrm{b} = (\rho_\mathrm{s} - \rho_\mathrm{w})/\rho_\mathrm{w}$). The parameters ρ_w ρ_w [kg m^{-3}] and g [m s^{-2}] denote the water density and gravity acceleration, respectively. The Shields stress τ^*, which is the nondimensional bed shear stress, is defined as:

$$\tau^* = \frac{\tau_b}{(\rho_s - \rho_w)gD_s}\frac{\tau_\mathrm{b}}{(\rho_\mathrm{s} - \rho_\mathrm{w})\mathrm{gD_s}} \tag{14}$$

where τ_b τ_b is the bed shear stress. The critical Shields number τ_c^* τ_c^* is the value of τ^* at the threshold of particle motion, which was regarded as constant (

0.03) for simplicity.

Assuming that the stream flows in a uniform steady condition, the bed shear stress τ_b τ_b is calculated as : (Chatanantavet and Parker, 2009):

$$\tau_{b\mathrm{b}} = \rho_{w\mathrm{w}} C_f^{1/3} g^{2/3} \left(\frac{Q_w}{W}\frac{\mathrm{Q_w}}{\mathrm{W}}\right)^{2/3} S^{2/3} \tag{15}$$

where C_f denotes the bed friction coefficient. Q_w Q_w [m^3 s^{-1}] and W [m] represent the water discharge and the width of the river, respectively. S indicates the bed slope.

Water discharge Q_w Q_w is determined by the following equation (Whipple and Tucker, 1999):

$$Q_{w\mathrm{w}} = k_\mathrm{SFDM}\bar{P}A \tag{16}$$

where k k_SFDM is a discharge coefficient representing rainfall variability, and $\bar{P}$ [m s^{-1}] denotes the average precipitation per unit area. A [m^2] represents the drainage area. Because the amounts of precipitation causing bedrock erosion are expected to be significantly larger than the average condition, the discharge coefficient k k_SFDM is also expected to be considerably greater than unity.

Assuming that the bedload sediment supply from the tributaries of the stream is proportional to the volume of the eroded material in the drainage area (Chatanantavet and Parker, 2009), the bedload discharge per unit width q_s q_s domain is obtained as:

$$q_{s\mathrm{s}}(x) = \frac{1}{W(x)}\left(q_s(0)_\mathrm{s}(0)W(0) + a\int\frac{dA}{dx}E(x)dx\right) \tag{17}$$

where x [m] is the streamwise distance from the upstream end of the calculation domain, and $q_s(0)$ $q_\mathrm{s}(0)$ is the bedload sediment supply at the upstream end. The ratio of the bedload to the total sediment supply is represented by a. In this study, we set $a = 0.14$ based on a previous study of Takayama (1965).

The sediment supply per unit width at the upstream end is assumed to be in a steady state, where the erosion rate E_{eq} E_{eq} is equal to the uplift rate of the bedrock. The bedload sediment discharge $q_s(0)$ $q_{\mathrm{s}}(0)$ at the upstream end ($x = 0$) is written as:

$$q_s(0)_{\mathrm{s}}(0) = \frac{kA(0)E_{eq}}{W(0)}\frac{\mathrm{aA(0)E_{eq}}}{\mathrm{W(0)}} \tag{18}$$

where $A(0)$ and $W(0)$ denote the drainage area and the channel width at the upstream end, respectively.

The channel width W is estimated by the empirical formulation using the river discharge (Finnegan et al., 2005) as follows:

$$W = k_{w\mathrm{w}}Q_{w\mathrm{w}}{}^{0.5} \tag{19}$$

where k_w k_{w} is the uniquely determined coefficient for each tributary.

To calculate the steady-state ($E = U$) channel profiles, Eq. (11) was recast to solve for the channel slope S using Eqs. (1), (13), (14), and (15), and (19), which takes the form:

$$\mathrm{S_{eq,SFDM}} = \left[\frac{\mathrm{R_b g^{1/3} D_s k_w^{2/3}}}{\mathrm{C_f^{1/3} Q_w^{1/3}}}\left\{\tau_{\mathrm{c}}^{*}\right.\right. \tag{20}$$

$$\left.\left. + \left(\frac{\beta_0 \mathrm{q_s^2}}{5.7(\mathrm{R_b g})^{1/2}\mathrm{D_s}(\beta_0 \mathrm{D_s^{1/2} q_s} - \mathrm{k_s^{1/2}}\sigma_{\mathrm{t}}^2\mathrm{U})}\right)^{2/3}\right\}\right]^{3/2}. \tag{21}$$

3.2 Stream power models

We applied two types of the stream power model. One is the Area-based Stream Power Model (ASPM), which considers the lithologic strength of bedrocks (Campforts et al., 2020)bedrock according to its lithologic types Campforts et al. (2020). This model does not account for the effect of the sediment cover rate ratio on the river bed. The other is the Stream Power with Alluvium Conservation and Entrainment Model (SPACEM) , which considers both the (Shobe et al., 2017; Guryan et al., 2024). SPACEM incorporates both lithologic strength and the sediment cover rate (Guryan et al., 2024)sediment cover ratio.

The ASPM is represented by the following equation:

$$E = k_{a\mathrm{a}}L_{E\mathrm{E}}S^nA^m \tag{22}$$

where k_a k_{a} (m^{1-2m} yr^{-1}) is the erosional efficiency parameter excluding the influence of the lithological erodibility , and L_E erodibility of bedrock, and L_{E} is the relative lithological erodibility erodibility of bedrock index. The positive exponents m and n are empirical parameters depending on lithology, rainfall variability, and sediment load (Campforts et al., 2020; Whipple and Tucker, 1999). The erosional efficiency k_a k_{a} was determined by the a Bayesian optimization in this study. L_E L_{E} was determined using the value proposed in Campforts et al. (2020).

On the other hand, the SPACEM considers both the lithology and the sediment cover rate, SPACEM considers lithology and sediment cover ratio but does not consider the sediment tool effectexplicitly include sediment tool effects. This model considers the rates of erosion E_r and entrainment $E_s$$E_{\mathrm{r}}$ [m yr^{-1}] and entrainment E_{s} [m yr^{-1}], which relate to the sediment thickness on the riverbed. The following equation represents the erosion rate E_r: E_{r}:

$$E_{r\mathrm{r}} = K_{r\mathrm{r}}q_{w\mathrm{w,yr}}S^ne^{-H/H_*} \tag{23}$$

where K_r K_r [m^{1-2m} yr^{-1}] is the bedrock erodibility, q_w is the $q_\mathrm{w,yr}$ [m^2 yr^{-1}] is the mean annual water discharge per unit width$(=Q_w/W)$, H [m] is the thickness of the sediment cover, and H_* [m] is the bedrock roughness scale. K_r K_r reflects the bedrock strength. The entrainment rate of the sediment from the bed E_s E_s is represented as:

$$E_{s\mathrm{s}} = K_{sed\mathrm{sed}} q_{w\mathrm{w,yr}} S^n \left(1 - e^{-H/H_*}\right) \tag{24}$$

where K_{sed} K_sed [m^{1-2m} yr^{-1}] denotes the sediment erodibility. In this model, the cover ratio P_c P_c is determined as H/H_*. The sediment thickness H depends on the rate of sediment entrainment E_s and deposition $D_s$$E_\mathrm{s}$ and deposition D_s, so that the relationship is calculated as:

$$(1-\phi)\frac{\partial H}{\partial t} = D_{s\mathrm{s}} - E_{s\mathrm{s}} = \frac{q_s}{q_w}\frac{\mathrm{q_s}}{\mathrm{q_{w,yr}}} W_{s\mathrm{s}} - E_{s\mathrm{s}} \tag{25}$$

where ϕ and q_s q_s denote the sediment porosity and the sediment flux per unit width, respectively. W_s W_s is the grain settling velocity determined by the grain size $D_s$$D_\mathrm{s}$. In this study, q_s, q_w q_s was calculated using Eq. (17), (16). . The mean annual water discharge $q_\mathrm{w,yr}$ was calculated using mean annual precipitation rate $\bar{P}_\mathrm{yr}$ as follows:

$$\mathrm{q_{w,yr}} = \frac{\mathrm{k_{SPACEM}\bar{P}_{yr}A}}{\mathrm{W}} \tag{26}$$

where k_SPACEM denotes a discharge coefficient representing rainfall variability.

Assuming the steady-state $(E=U)$, the channel slopes can be calculated in the same manner as SFDM:

$$S_\mathrm{eq,SPACEM} = \left(\frac{q_sW_s}{K_{sed}q_w^2}\frac{\mathrm{q_sW_s}}{\mathrm{K_{sed}q_{w,yr}^2}} + \frac{U}{q_wK_r}\frac{\mathrm{U}}{\mathrm{q_{w,yr}K_r}}\right)^{1/n} \tag{27}$$

In this calculation, the grain settling velocity W_s W_s was assumed to be spatially constant in this model.

The value of K_r K_r for the most fragile rock type (i.e., tuff) was set to 1.0×10^{-5} according to (Guryan et al., 2024)Guryan et al. (2024). Assuming that this coefficient is proportional to the rock tensile strength, the bedrock erodibility $K_{\mathrm{r},i}$ $K_{\mathrm{r},i}$ for the ith rock type was determined as follows:

$$K_{\mathrm{r},i} = \frac{\sigma_{\mathrm{t},i}K_\mathrm{r,tuff}}{\sigma_\mathrm{t,tuff}}\frac{\sigma_\mathrm{t,i}\mathrm{K_{r,tuff}}}{\sigma_\mathrm{t,tuff}} \tag{28}$$

where $\sigma_{t,i}$ $\sigma_{\mathrm{t},i}$ and $\sigma_\mathrm{t,tuff}$ denote the tensile strengths of the ith rock type and tuff, respectively.

3.3 Optimization of model parameters

In this study, the discharge coefficient k k_SFDM, k_SPACEM and channel width coefficient k_w k_w were optimized to minimize the elevation differences between the actual river profile and the result of the model calculation. The objective function was defined as the root mean square (RMS) of the total elevation differences summed over the 5 tributaries.

$$RMS\mathrm{RMS} = \sqrt{\frac{1}{NM}\sum_{n,m=1}^{NM}\left(z_{nm}^O - z_{nm}^C\right)} \tag{29}$$

Table 2. A list of optimized parameters and their searched ranges.

model	params	range
SFDM	k k_{SFDM}	0–150
	k_w k_{w}	0–15 0–3 (channel specific value)
ASPM	k_a k_{a}	0–15
SPACEM	k k_{SPACEM}	0–15

z^O_{nm} and z^C_{nm} represent the observed and calculated elevation, respectively. The optimal parameters were determined using Optuna (Akiba et al., 2019), which is an optimization framework based on Bayesian optimization, a method that efficiently explores the optimal solution by sequentially updating the posterior distribution based on the evaluation results of a probabilistic model.

This study performed the Bayesian optimization with 10,000 trials to fit the model outputs to the observed river longitudinal profiles. As a result, the optimal parameters were obtained: k and k_w k_{SFDM} and k_{w} for SFDM, k_a k_{a} for ASPM, and k k_{SPACEM} for SPACEM. In the case of SFDM, k_w k_{w} was individually optimized for each tributary, while the remaining parameters were treated as common values across all tributaries. The search ranges for these parameters are summarized in Table 2. Note that the uncertainties associated with the optimized parameters were not explicitly evaluated in this analysis.

In addition, we performed a sensitivity analysis of the parameters used in SFDM, ASPM, and SPACEM that were adopted from the literature. Each parameter was varied within a reasonable range (Table 2), and the model was re-optimized for each parameter set using Bayesian optimization with Optuna to minimize the RMS error between the observed and calculated topography of the Gohyaku River.

4 Methods for topographic and geologic analysis

4.1 Topographic analysis

The topographic elevation, slope, and drainage area along the channels of the surveyed rivers were extracted from the digital elevation model (DEM) of the Geospatial Information Authority of Japan. First, 10-m-mesh DEM data of the surveyed tributaries were utilized to calculate the flow accumulation. The Deterministic 8 algorithm, where in which water at each pixel is assumed to flow in the maximum dip direction direction of maximum downslope gradient, was employed to obtain the drainage areas (O'Callaghan and Mark, 1984). The pixels exceeding Flow paths draining more than 7×10^4pixels in the drainage areas km^2 were regarded as river channels. The channel slope was then calculated along the channel path from the elevation data. The geographical information system software SAGA GIS was used for these procedures (Conrad and Böhner, 2015).

The normalized steepness index k_{sn} k_{sn} was used to clarify the effect of the bedrock strength on the channel steepness in all the investigated tributaries. This parameter is defined as the upstream area-weighted channel gradient (Campforts et al., 2020;

Wobus et al., 2006):

$$k_{sn\mathrm{sn}} = SA^{\theta} \tag{30}$$

The exponent θ is the concavity index, which is generally set to 0.45 (Wobus et al., 2006). Empirical studies show that concavity indices typically range from 0.3 to 0.7 (Tucker and Whipple, 2002; Goren and Shelef, 2024). In this study, we adopted a value of 0.36, which was optimized for the study area.

A chi plot is often used to identify whether the river profile is in the Chi plots are commonly used to assess whether uplift rate and bedrock erodibility are spatially uniform (Perron and Royden, 2013). Under steady-state , or not (Perron and Royden, 2013)conditions with uniform erodibility, river profiles are linear in chi space; deviations from linearity indicate spatial variations in uplift rate or erodibility. It is a coordinate transformation to linealize linearize the river profile determined by:

$$\chi = \int_{x_b \mathrm{x_b}}^{X} \left(\frac{A_0}{A(x)}\right)^{m/n} dX \tag{31}$$

where X is the distance from downstream, and x_b x_{b} is a base level. A_0 denotes a reference drainage area, and the drainage area at the downstream end is set in this study.

4.2 Measurement of Rock Strength

The lithologies of the bedrocks were distinguished by the naked eye bedrock were distinguished in the field survey and were recorded in the geological route map of the researched tributaries. The 1:50,000 and 1:200,000 geologic maps published by the Geological Survey of Japan were also used to distinguish the lithologies where the bedrocks were bedrock was not exposed on the channels.

Then, the tensile strengths of the bedrocks various bedrock materials of the representative lithologies were sampled and measured using the Brazilian tension splitting test (Vutukuri et al., 1974). Before the analysis, the specimens were submerged in the water under a vacuum condition for 12 weeks until their weight did not change. This procedure is was selected because the goal was to measure the bedrock strength in the wet conditiona wet condition. We justify this approach because it has been shown that the water saturation condition affects the content in the pore space of bedrock can affect the rock tensile strength (Bao et al., 2021).

In this test, the specimens had a diameter of 50 mm and a length of 25 mm (Society, 2016). The load was applied to the specimen at 1 μm s^{-1} until a crack formed, and the maximum load P_{max} P_{max} [kN] at the moment of failure was measured.

The tensile strength σ_t σ_{t} was then determined using the following Eq. (32).

$$\sigma_{t\mathrm{t}} = \frac{2P_{max}}{\pi DL}\frac{2\mathrm{P}_{\mathrm{max}}}{\pi\mathrm{DL}} \times 1000 \tag{32}$$

where D (mm) and L denote the diameter and length of the specimen, respectively.

The gneiss measured in this study had a schistosity plane, and the measurement values can exhibit schistosity planes in gneiss can result in large variability depending on the surface on which the failure occurred. We assumed that the riverbed failure occurred along the weak plane, so we adopted not the average value, but the value when the specimen was cropped along the weak plane.

4.3 Automated grain size measurements of riverbed gravels

The grain sizes of the riverbeds were measured from the drone-derived 3D point cloud datataken by the drone (Steer et al., 2022). . In recent years, the methods for automated grain-size analysis have been rapidly developing (e.g., Soloy et al., 2020; Steer et al., 2022; Mair et al., 2024). Among those studies, the method proposed by Steer et al. (2022) can measure the three axes of the grains from 3D point cloud data obtained by drone photogrammetry, allowing the grain axes lengths and the volume of grains to be measured. In this study, we adopted the volume-based metric for the representative grain size, so that the G3Point method Steer et al. (2022) was employed.

The measurement procedures were as follows. (1) The drone (DJI Air-2s) photographed approximately 100–200 m^2 areas of the riverbeds. (2) The 3D point clouds exhibiting riverbed surface morphologies were produced by the Structure from Motion algorithm using the Agisoft Metashape. (3) The triaxial ellipsoid Triaxial ellipsoids fitted the morphology of each gravel to measure grain diameter the diameters of the grains using the software G3Point (Steer et al., 2022).

This studyIn this study, we defined the representative grain diameter $\bar{D_s}$ $\bar{D}_\mathrm{s}$ as the mean of the diameter of the spheres in the weighted arithmetic mean (D_{50}), which are equal to the fitted tri-axial ellipsoids in volume.

Since the G3Point program can analyze a maximum of 1 million points at a time, this study we split the analysis area into two or three non-overlapping rectangular regions with a width of 5 m or less, and the . The mean values of these subareas were then used as the measurement result of the results of the measurements in the surveyed area. We cropped the water surface contained in the 3D point cloud manually because G3Point sometimes misidentified the water surface as the grain surface. In the G3Point method, 10 points are required to fit an ellipsoid to a grain, so the measurable minimal grain size is 1–2 cm.

To estimate the mean diameter D_s D_s of the riverbed gravels along each stream, the measured values were interpolated with Sternberg's law Eq. (33) (Sternberg, 1875): (Sternberg, 1875; Snelder et al., 2011; Miller et al., 2014):

$$D_x = D_0 \exp(-\alpha_{d\mathrm{d}} x) \tag{33}$$

where D_0 is the grain diameter at the origin, and α_d α_d is the change rate of the mean diameter. This study Here, we assumed that the river gravels fine downstream so that α_d is supposed to (Parker, 1991), so that α_d should be a positive value. These parameters D_0 and α_d were estimated α_d were estimated from the mean of the measured values using the least-squares method.

The grain sizes of the riverbed gravels were also measured manually at the two locations (Sakura River and Gohyaku River) to evaluate the accuracy of the automated measurements. In this manual measurement, the longest (a), intermediate (b), and short shortest (c) axes were measured, and . First, we delineated a several-square-meter area on a river bar using spray paint. Within this area, we measured the sizes of clasts that were visually identifiable from a vertical viewpoint, had exposed surfaces, and possessed a short axis of at least 1 cm. Then the results were compared with those obtained by the G3Point program.

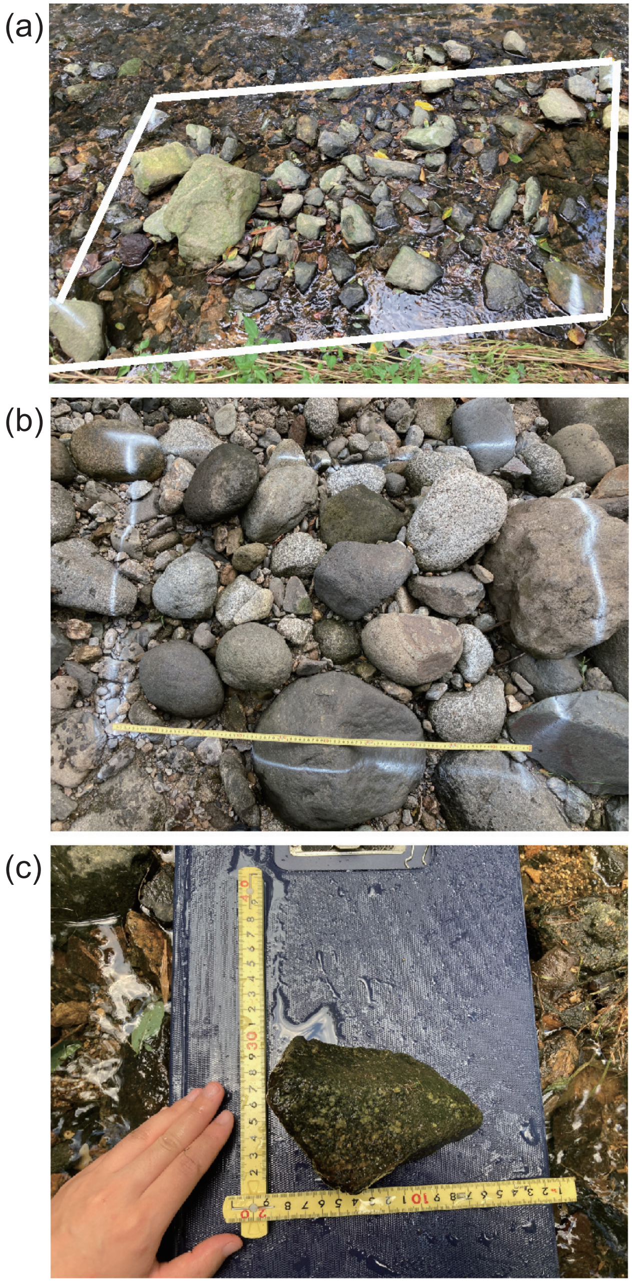

Figure 2. Photos of river gravels. (a) Photograph of gravels at Sakura River, the Tamura-Country, Fukushima. The area surrounded by the white lines was about 1.0×2.5 m. (b) Photograph of gravel at Gohyaku River, the Koriyama City, Fukushima. The area size was 0.8 m×1.0 m. (c) Manually measuring the gravelsgravel size.

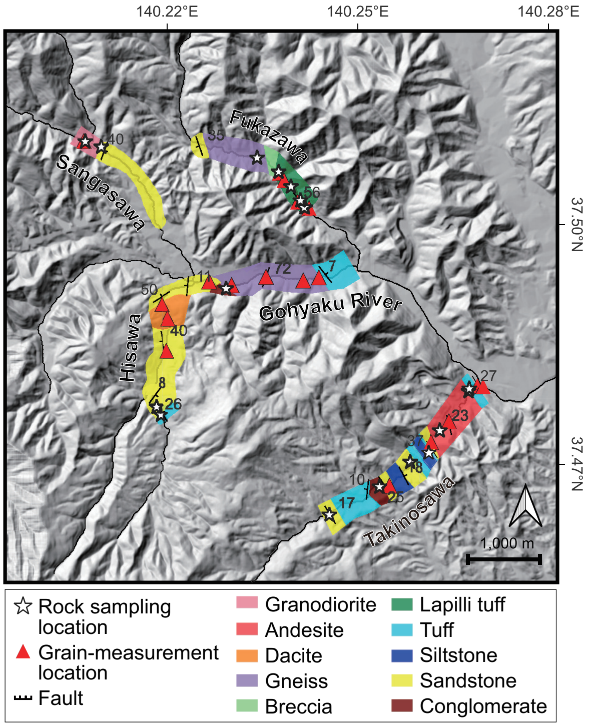

Figure 3. Route map in the researched area. The data classification of lithologic distributions in the unsurveyed areas were referred was inferred from previous studies (Kubo et al., 2003; Yamamoto and Sakaguchi, 2023)(Kubo et al., 2003; Yamamoto and Sakaguchi, 2023). The star mark represents the location of the rock sampling. The pink triangle represents the location where the grain size distributions were measured using the drone. DEM data was were obtained from the Technical Report of the Geospatial Information Authority of Japan.

5 Results

5.1 Topography and geology of the surveyed channels

We identified ten types of sedimentary, pyroclastic, gneiss, and igneous rocks exposed on the riverbed of five tributaries of the Abukuma River (Takinosawa, Hisawa, Fukazawa, Sangasawa, and Gohyaku Rivers). The sedimentary rock is subdivided into conglomerate, massive sandstone, and siltstone. The pyroclastic rock includes rocks include volcanic breccia, lapilli tuff, and tuff. The igneous rocks are granodiorite and andesite. The volcanic and pyroclastic rocks are distributed in the northeastern region where Takinosawa and Fukazawa exist. The granodiorite is exposed in the northwestern region (Sangasawa). A major fault exists in the upstream region of Gohyaku River, while no significant topographic change at the fault was observed in the field. A gentle synclinal structure with an NNE-SSW trending fold axis was observed in the study area, whereas an anticlinal structure was also observed upstream of Takinosawa and a further one in a south tributary. These clinal structures were all trending NNE-SSW.

The result results of topographic analysis and geological survey indicated that the river profiles did not vary significantly in slope at the lithologic boundaries. The river course does not show significant changes at fault or fold locations, suggesting that tectonic structures exert limited control on channel morphology in this area. Figure 4 exhibits the channel longitudinal profiles of the surveyed tributaries extracted from the DEM, and where the lithologies identified through the field surveys were plotted as the symbols and colors. Most of the rivers have weakly concave-downward concave-upward smooth profiles. The channel slopes in the surveyed region range from 0.02 to 0.05.

Several knickpoints can be observed in Sangasawa, Fukazawa, and Gohyaku River, but they do not correspond to the lithologic boundaries. The knickpoints are associated with lithological boundaries. In Takinosawa, a knickpoint occurs at the boundary between sandstone and conglomerate, with a thin tuff layer in between. The average channel slope in the conglomerate reach is 0.056, whereas that in the upstream sandstone reach is 0.052, yielding a slope difference of only 0.004 across the lithologic boundary. Other minor knickpoints that coincide with lithological boundaries exhibit a trend opposite to the commonly expected pattern, in which channel gradients are steeper in harder bedrock and gentler in weaker lithologies. In Fukazawa, knickpoints occur at both the sandstone-gneiss and breccia-tuff boundaries. However, in both cases, softer rocks (sandstone and breccia) are located upstream, where channel slopes are steeper, whereas harder rocks (gneiss and lapilli tuff) occur downstream, where slopes are lower.

There are also knickpoints that do not correspond to lithologic boundaries. The knickpoint in Fukazawa and Gohyaku River are located in the range where the gneiss is distributed. A small knickpoint is also observed in the middle of Sangasawa . This point corresponds to the Sangasawa corresponds to a significant change in the drainage area of the river, while the . The lithologic boundary between the granodiorite and sandstone is located slightly about 120 m downstream of this knickpoint.

The check dams were located in Hisawa and Sangasawa. The The knickpoint downstream of Hisawa coincides with the location of the check dam. No significant topographic change at the fault was In Sangasawa, a check dam is located 10 m downstream of the confluence, whereas the step observed in the field. topography within the granite occurs upstream of the dam. Several knickpoints are located within the same lithology, such as gneiss in the Fukazawa and Gohyaku rivers, even where no significant change in drainage area or check dam is observed.

The chi-plot results (Fig. 5) did not show typical knickpoints that correspond to all tributaries. Takinosawa The Takinosawa River has a knickpoint that is absent in other tributaries. The steepness of Takinosawa, Hisawa, and Gohyaku River over $\chi = 20,000$ was almost the same; on the other hand, that of Fukazawa and Sangasawa was much steeper.

5.2 Bedrock strengths

The measured results of the bedrock strengths indicated that igneous and metamorphic rocks exhibited significantly larger tensile strength than sedimentary rocks (Fig. 3; Tab. 3). The strengths of igneous and metamorphic rocks ranged from 4.3 to 8.2 MPa. The Strength measurements accomplished on the dacite at Fukazawa demonstrated the maximum tensile strength yielded a maximum value of 8.2 MPa, which was more than 18 times larger than the minimum tensile strength of tuffs (0.46 MPa). The sedimentary rocks ranged in tensile strength from 0.4 to 2.4 MPa. They demonstrate variation in their strength depending on the location. The sandstones along Takinosawa were harder than those along Sangasawa.

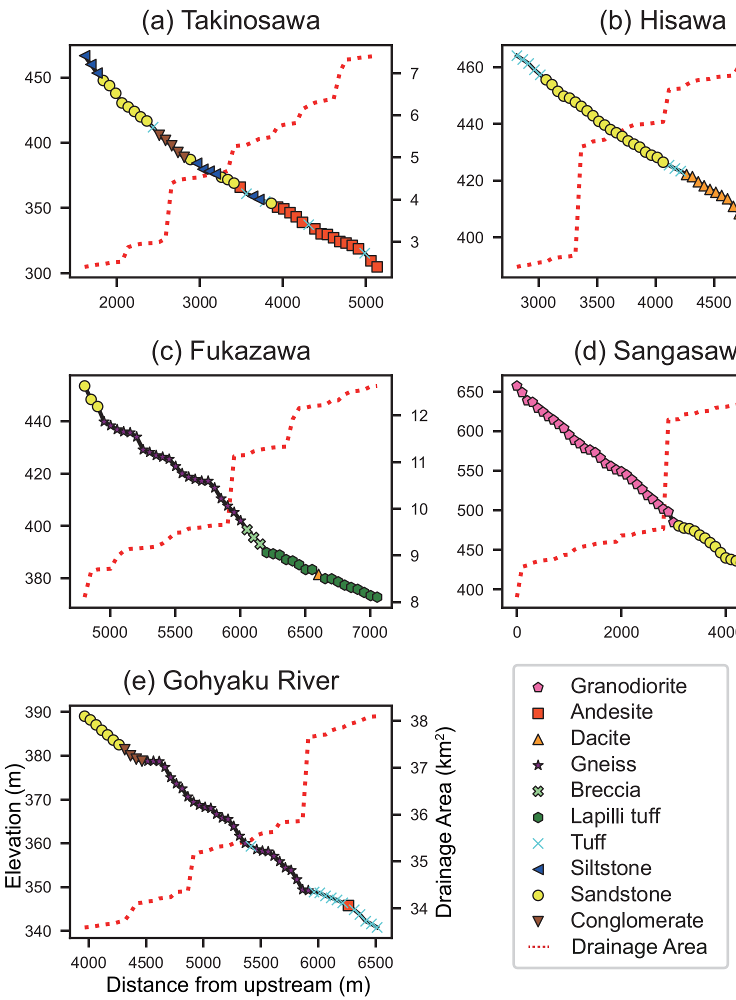

Figure 4. River profiles extracted from the DEM and the lithology data obtained through field surveys—the point on the channel positioned at 10-m intervals. The upstream end was at the channel's endpoint on the map.

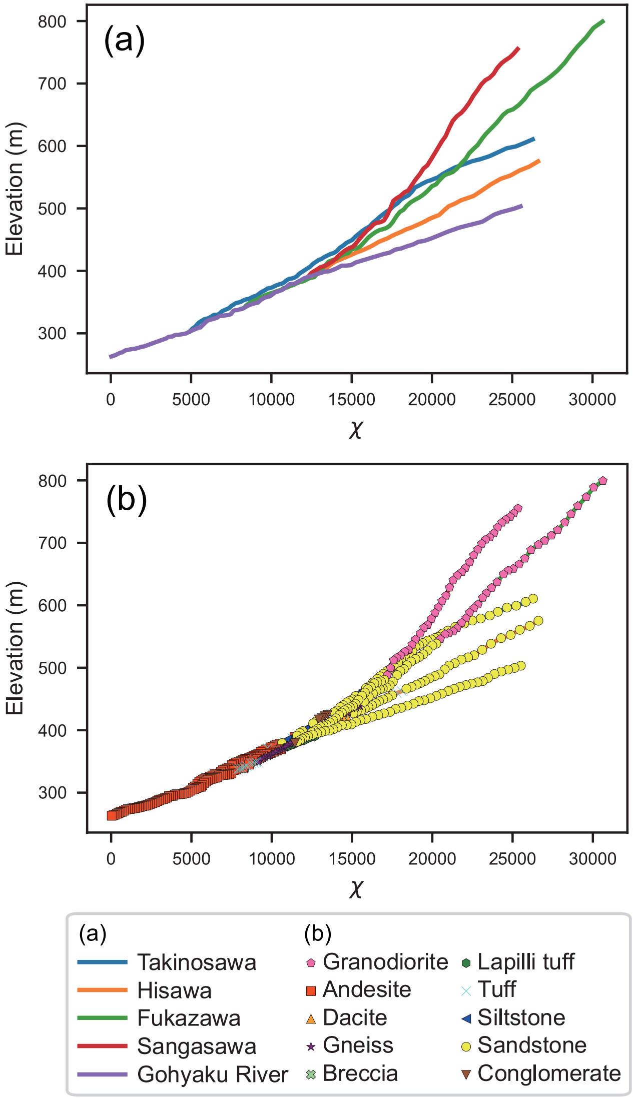

Figure 5. Channel profiles represented by the as chi plotplots. The x-axis represents the chi value calculated by using Eq. (31). In this study, the concavity index m/n was assumed to be 0.36 to draw for constructing the chi plotplots. (a) Chi plots of individual tributaries. (b) Chi plots of individual tributaries colored by lithology.

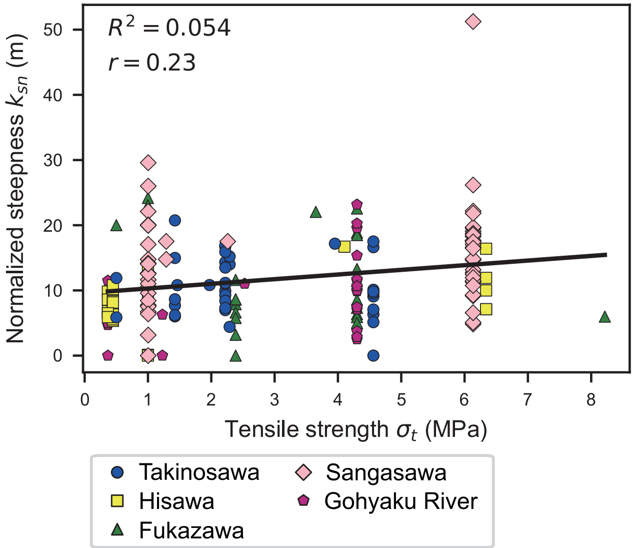

Figure 6. The relationship between normalized steepness and bedrock tensile strengths. Rock tensile strength is weakly correlated with the river steepness.

The correlation relationship between channel slope and bedrock tensile strength was weak , with exhibited a weak correlation, with a correlation coefficient r of 0.23 and an R^2 value of 0.061.The channel slope slightly increased, along with an increase in tensile strength. The range of channel slope at each tensile strength was large0.054 (Fig. 6). The p-value was 0.0025 ($p < 0.05$), indicating that the correlation is statistically significant.

5.3 Grain size distribution along river channels

5.3.1 Comparison between automated and manual measurements

The median grain size of riverbed gravels automatically measured by the G3Point closely matched well with manual measurements (Fig. 7). The median grain size was 0.21 m for automated measurements and 0.19 m for manual measurements in the Gohyaku River. Similarly, in the Sakura River, these values were 0.18 m and 0.17 m, respectively. Generally, the G3Point program accurately estimates the length of the b-axis. For the a-axis length, the cumulative curves of automated and manual measurements were similar in the regions below the 50th percentile. However, they diverge in the larger grain size regions regions where larger grains occur, indicating that the automated measurements are generally accurate except for larger cobbles and boulders. The automated measurements erroneously overestimate the c-axis of gravels (Fig. 7 (b), (d)). Nevertheless, the median grain size measured by the fitting of ellipsoids using G3Point differed by only 0.02 m from the manual measurement results.

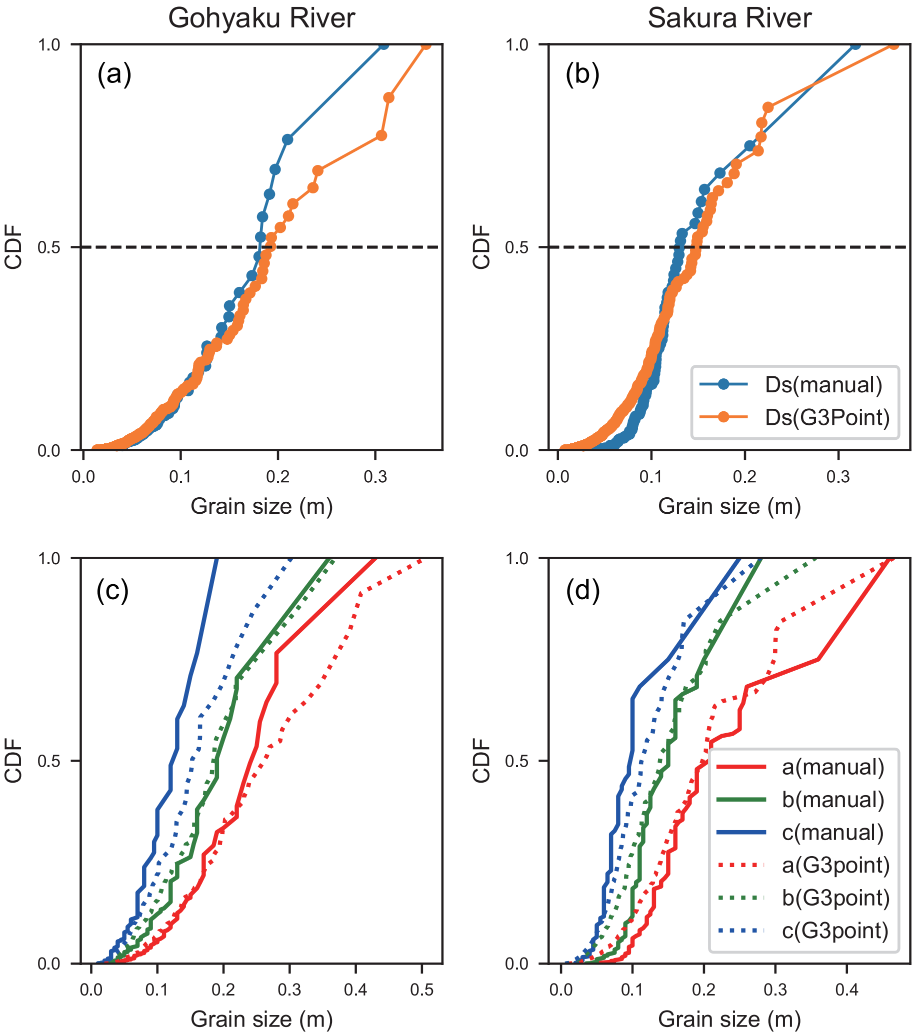

Figure 7. Comparison between automated (G3Point) and manual grain size measurements. The curves represent cumulative distribution functions (CDF), with the vertical axis indicating cumulative volume (%). Orange plots show grain size data obtained using G3Point, while blue plots represent manually measured data. The dashed line indicates the median grain size (D_{50}). The D_{50} value derived from G3Point was slightly larger than that from manual measurements, with a difference of approximately 0.02 m.

Table 3. Measured Values of rock tensile strength σ_t σ_t measured in this study. The asterisk mark ($*$) indicates that the tensile strength values were not measured at the tributary, and the values were substituted by those measured in other tributaries.

Rock type	Location	σ_t σ_t [MPa]
Granodiorite	Sangasawa	6.1
Dacite	Hisawa	6.3
	Fukazawa	8.2
Andesite	Takinosawa	4.5
Gneiss	Fukazawa, Gohyaku River	4.3
Breccia	Fukazawa	0.5*
Lapilli tuff	Fukazawa	2.4
Tuff	Takinosawa	0.5
	Fukazawa	0.4
	Hisawa, Gohyaku River	0.4*
Conglomerate	Takinosawa	2.3
	Gohyaku River	1.3
	Sangasawa	1.3*
Sandstone	Takinosawa	2.2
	Hisawa	0.4
	Fukazawa	1.0
	Sangasawa	1.0*
Siltstone	Takinosawa	1.4

5.3.2 Grain size distribution

Spatial distributions of grain size along river channels were examined from the D_{50} values obtained in measured points (Fig. 8). The median grain diameters of riverbed gravels in the study area ranged from 0.4 to 0.7 m. This value is reasonable in the field because the estimated minimum flow depths using $\tau^* = \dfrac{hS}{R_b D_s}$ range from 0.5–1.0 m across the study tributaries under $\tau^* = 0.05$ and $R_b = 1.65$, and these depths are plausible during high-flow events that dominate bedrock erosion.

Fukazawa and Takinosawa exhibited a downstream fining trend, although the spatial variation of the grain size grain sizes in Takinosawa was much weaker than in Fukazawa. Other tributaries (Hisawa, Sangasawa, Gohyaku River) exhibited constant grain distributions, and thus the change rate α_d α_d in the grain size trend (Eq. 33) was almost zero. As the median grain diameter decreases, the grain size variation also tended tends to decrease. In general, grain distribution becomes discontinuous at the point of the check dam, but these grain distribution results did not consider the reflect the effects of the dams for simplicity.

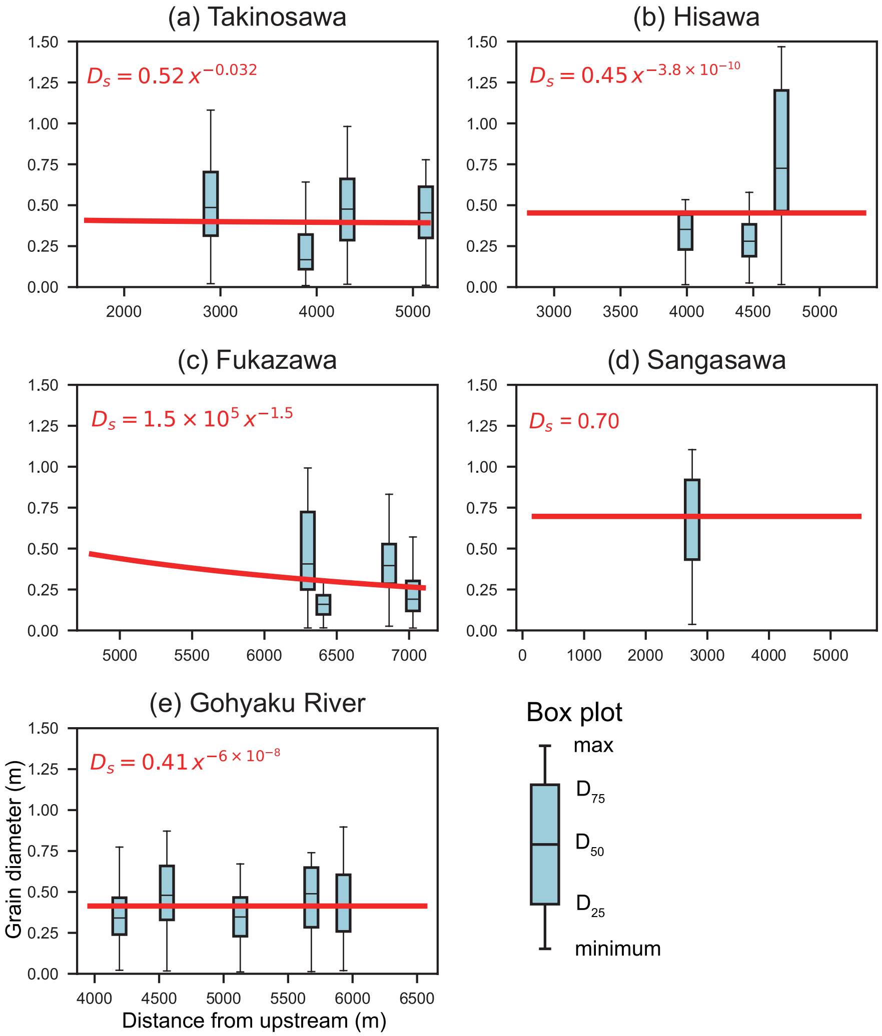

Figure 8. Measured results of grain size distributions for each tributary. Blue box plots represent the median and quantile ranges of the grain diameter. The red line represents the estimated spatial distribution of D_{50}.

Table 4. Input parameters of the sediment-flux-dependent model.

Input parameters	SFDM	params	ASPM	
Uplift rate U	375 m Myr^{-1}	Uplift rate	375 m Myr^{-1}	375
Erosional efficiency β_0	0.0001	Erosional coefficient k_a k_a	5.8	
Average precipitation rate $\bar{P}$	4.07 $\times 10^{-8}$ m s^{-1}	Discharge coefficient k Average precipitation rate $\bar{P}_\mathrm{yr}$	–	3.11.
Grain diameter D_s D_s	0.3 – 0.7 m	Sediment erodibility K_{sed} Settling velocity W_s	–	1.1×0^{-5} 4
Tensile strength σ_t σ_t	0.4 – 8.2 MPa	Lithological erodibility L_E, K_r $L_\mathrm{E}, K_\mathrm{r}$	0.3 – 1.7	5.3
				1.
Nondimensional critical shear stress τ_c^* τ_c^*	0.004	Drainage area exponent m Sediment erodibility K_sed	0.5 –	0.75 1.
Bedrock roughness k_b k_b	0.0032	Bedrock roughness H_*	–	
Friction coefficient C_f	0.004	Slope exponent n	1.0	
Discharge coefficient k Bedload ratio a	0.14	Drainage area exponent m	0.5	
Discharge coefficient k_SFDM	120.4	Settling velocity W_s Discharge coefficient k_SPACEM	–	42
Channel width coefficient k_w k_w		Bedrock roughness H_*	– 1.0 m	
Takinosawa	1.7 1.5			
Hisawa	1.1			
Fukazawa	2.2			
Sangasawa	1.0			
Gohyaku River	1.5 1.7			

See each value of D_s and σ_t in Fig. 8 and Tab. 3.

5.4 Model predictions for bedrock river profiles

The numerical experiments using the sediment-flux-dependent well reproduced model reproduced well the actual river profiles . (Fig. 9, red line). The channel width coefficient $k_w k_\mathrm{w}$, which was optimized for the calculation, ranged from 1.0 to 2.12.2, and the optimized value for the discharge coefficient k was 117.2. Using optimized k_w, k, and k_SFDM was 120.4.

Bankfull widths predicted using Eq. (19) with the optimized values of k_w and k_SFDM are consistent with field observations and with estimates derived from 3D point-cloud datasets of the riverbeds. For Takinosawa, the predicted bankfull width is approximately 5–9 m, channel width becomes 5 m– 9 m at Takinosawa, 5 m – whereas the observed width is about 7 mat Hisawa, 13 m – 16 mat Fukazawa, 4 m – 9 mat Sangasawa, . Similarly, the predicted widths for Hisawa and the Gohyaku River are approximately 5–7 m and 22 m– 24 m at Gohyaku River. 22–24 m, respectively, which are comparable to the observed widths of about 10 m and 15–20 m. For Fukazawa and Sangasawa, the predicted bankfull widths are approximately 13–16 m and 4–9 m, respectively. Direct measurements of bankfull width were not available for these rivers.

The Both the observed and modeled river slopes profiles exhibited consistently smooth profileslongitudinal trends, regardless of underlying bedrock strength (Fig. ??9). The mean squared error between the SFDM and actual profile was 3.5 m, which was the best among the three models (SFDM, ASPM, and SPACEM) examined in this study. The model

The SFDM prediction for Sangasawa reproduced the knickpoint due to the remarkable change in drainage area. Takinosawa had has a concave-upward profile, and the model simulated a similar profile due to the downstream fining grain size distribution. However, the model failed to reconstruct the step-like structures knickpoints of the river profile observed in Fukazawa and Gohyaku Rivers. This discrepancy was particularly pronounced in areas underlain by hard bedrocks such as granodiorite and gneiss.

Thus, although the SFDM did not capture the fine topographical changes on a scale of a few hundred meters, it accurately reproduced the overall characteristics of the bedrock river profiles.

In contrast to the SDFM, the profiles predicted by the stream power models (ASPM and SPACEM) did not agree with the actual profiles. Their predictions reflected the bedrock strengths clearly in slopes clearly reflected the controls of variations in bedrock strength through the slope profiles (Fig. ??9, red dashed-dot pattern and dashed line). The optimized erosional coefficient for ASPM k_a k_{a} was 5.8 [yr^{-1}], and the optimized discharge coefficient k k_{SPACEM} for SPACEM was 3.03.1. The ASPM profile exhibited a remarkable change in slope at the lithologic boundary of the river bedrocksbedrock types. Especially in Sangasawa, where the contrast in bedrock strength was most pronounced, the ASPM predicted upstream steepness distributed that upstream steepness in granodiorite was 9 times steeper than downstream steepness distributed greater than the downstream steepness in sandstone. The actual Sangasawa slope change was very small, so that this ASPM result was significantly different from the actual profile (Fig. ??9).

The profiles predicted by the SPACEM still deviated from the actual profiles (Figs. ?? and ??Fig. 9), although they were smoother than those of the ASPM. In Sangasawa, the modeled slope of SPACEM changed at the lithological boundary, with the upstream slope being about four times steeper than the downstream slope. The mean squared error between the ASPM and the actual profiles was 21.7, and that of the SPACEM was 13.2.

The results of sensitivity analysis exhibited that in the SFDM, variations in the nondimensional critical shear stress, friction coefficient, and bedload ratio have only minor effects on river profiles, whereas changes in erosional efficiency produce slight gradient variations associated with lithological contrasts but overall stable results (Figs. S1–S8). In contrast, the ASPM exhibited strong parameter sensitivity: river profiles deviate markedly from observations when the slope exponent n exceeds 1.5 or when the drainage area exponent m is below 0.5, indicating that the adopted values ($n = 1.0$, $m = 0.5$) lie within a stable range (Figs. S9–S12). In the SPACEM, channel gradients were less sensitive to n than in the ASPM and remained stable for $n \geq 0.7$, while variations in sediment erodibility K_{sed} within reported ranges caused only minor changes in gradients and RMS (Figs. S13–S18). Overall, the sensitivity analysis confirms that the parameter values used in this study fall within stable regimes and yield results consistent with the observed topography.

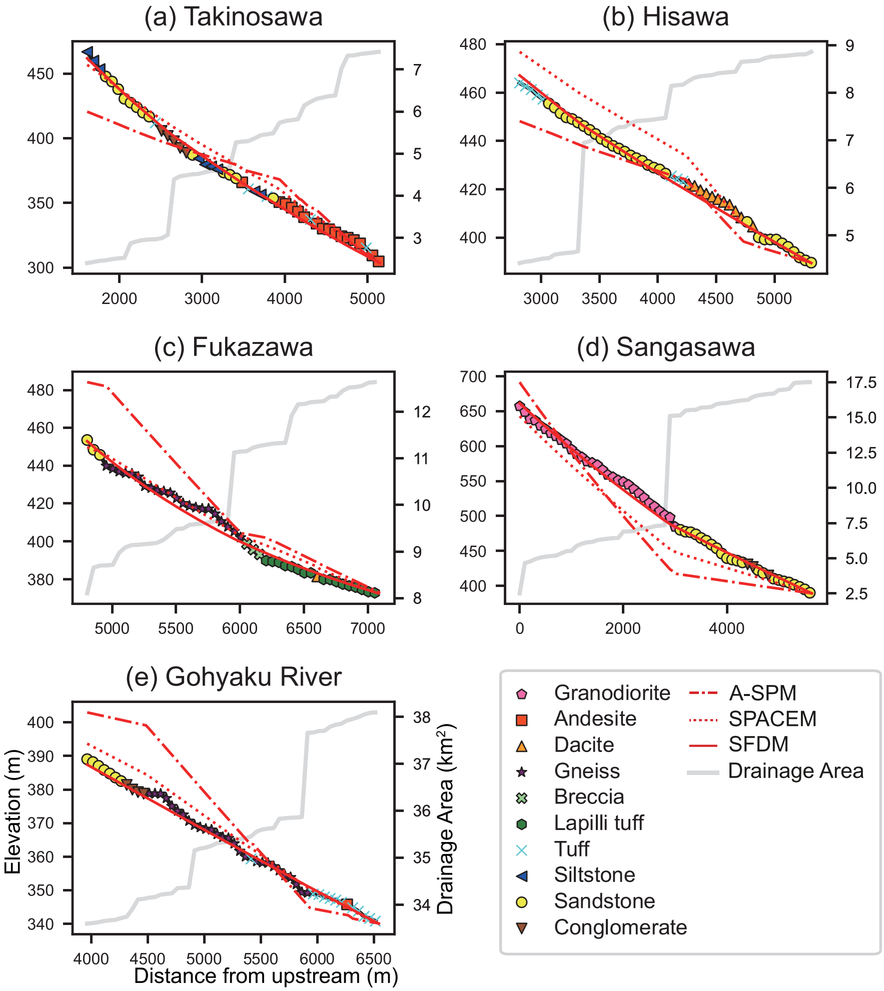

Figure 9. Results of reproduction of the river longitudinal profiles using a sediment-flux-dependent modelASPM, SPACEM, and SFDM. The model was These models were calculated on a 10-meter interval grid under the condition that the erosion and the uplift rates are balanced (steady state). The red line represents represent the steady-state model profile of SFDM. The colored plots represent the actual river profiles and lithologies. The dash-dot line represents the steady-state profile calculated by ASPM, and the red dot line represents that by SPACEM. The grey line represents drainage area.

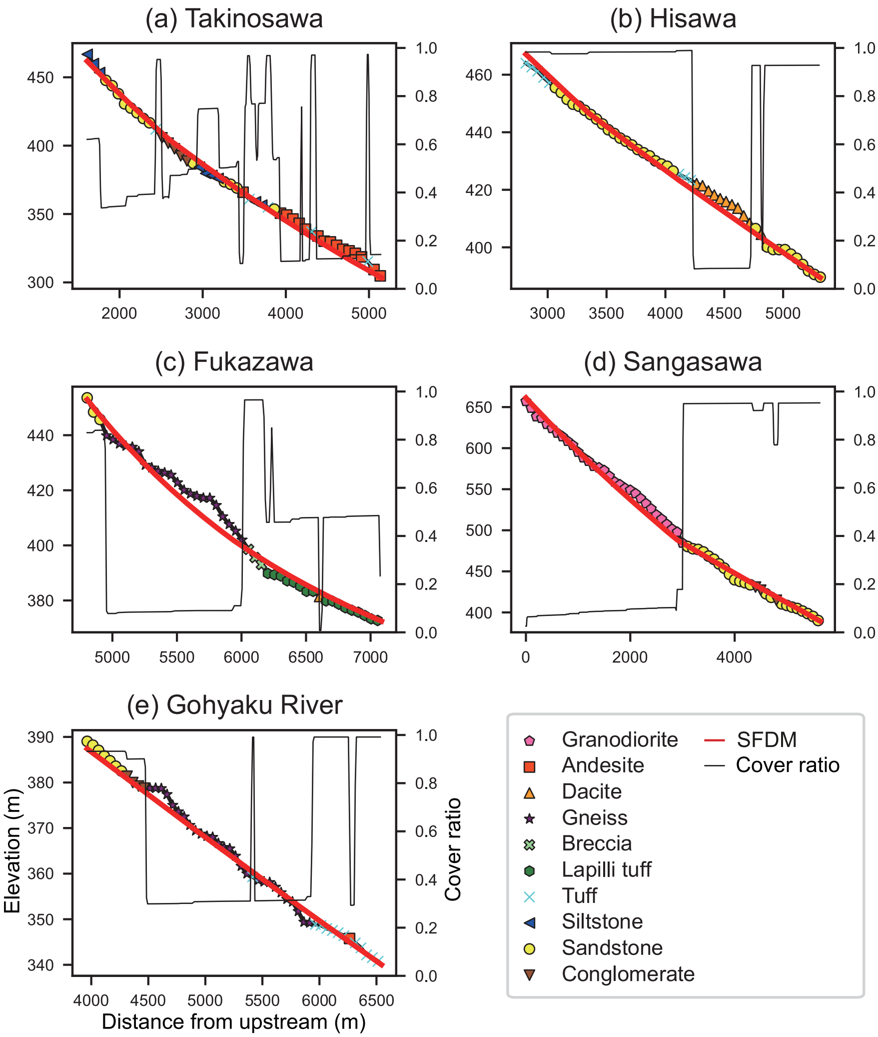

Figure 10. The result Cover ratio results of the calculation calculations by ASPM and SPACEMEq. (12), with SFDM results. The red black line represents the steady-state profile calculated by SPACEM, and the dashed red line represents that by ASPMcover ratio at each site. The models were calculated on cover ratio shows a 10-meter interval grid, the same as SFDMclear correspondence with lithology.

6 Discussion

6.1 Why bedrock strength has little influence on local slopes in river longitudinal profile

The field measurements in this study indicated that the bedrock strength has a limited influence on the river longitudinal profiles. Hayakawa and Oguchi (2009), Brocard et al. (2015), and Takahashi (2025) also suggested that the influence of lithological erodibility on the river profile was small. This study proved this fact clearly by measuring The measurement of bedrock tensile strength included in the present analysis serves to justify this observation.

The numerical experiments implied that these smooth river profiles over different lithologies are imply that the smoothness of the longitudinal profiles of these rivers, in which clear breaks corresponding to a change in lithology are not seen, is attained by the sediment covering sediment-cover effect (Fig. 11). The sediment-flux-dependent model predicted that the sediment cover ratio mitigated the effect of bedrock strength. Through the cover ratio being higher in soft rocks and lower in hard rocks, erosion is suppressed in soft rock areas, and erosion is promoted in hard rock areas . (Fig. 10). Eq. (21) indicates that the bedrock strength appears only in the denominator of the first term on the right-hand side of the equation. However, in this equation, the product of the square root of hydraulic roughness $k_s^{1/2}$ $k_\mathrm{s}^{1/2}$, the squared rock tensile strength σ_t^2 σ_t^2, and the uplift rate U (375 m Myr^{-1} in this study) has a value in the range the order of 10^{-11} to 10^{-13} [$\mathrm{kg}^2\mathrm{m}^{-1/2}\mathrm{s}^{-5}$], while the term of the product of coefficient β_0, the grain size $D_s^{1/2}$ $D_\mathrm{s}^{1/2}$, and sediment supply rate q_s q_s is the order of 10^{-10} [$\mathrm{kg}^2\mathrm{m}^{-1/2}\mathrm{s}^{-5}$]. Thus, it is clear from the equation that the value of rock tensile strength has little effect on the resulting slope. The mechanical explanation for controlling the sediment cover ratio in relation to lithology is as follows.

Considering the cover ratio, even minor changes in river slope can substantially alter erosion rates, effectively mitigating the influence of the bedrock strength. The sediment cover ratio on the bedrock surface increases as the sediment transport capacity approaches the actual sediment supply. Conversely, the cover ratio P_c P_c decreases when the sediment supply is limited or when transport capacity increases. This dynamics is explicitly considered in the sediment-flux-dependent model, in which P_c P_c is formulated as the ratio of sediment supply q_s q_s to the transport capacity q_t q_t (Sklar and Dietrich, 2004; Chatanantavet and Parker, 2009). Here, the sediment supply is primarily governed by upstream conditions, while the transport capacity q_t q_t is controlled by the bed shear stress, which increases with the channel slope S. Therefore, under constant sediment supply, the cover ratio P_c P_c is slope-dependent (Fig. 11). This dependence is particularly pronounced at low gradients, where the bed shear stress is near the threshold for the gravel mobilization, making P_c P_c highly sensitive to small changes in slope (Fig. 12). Because the sediment cover shields the bedrock from direct impact by bedload particles, even slight variations in slope—and thus in cover ratio—can lead to significant differences in erosion rates . (Fig. 10).

As a result, river longitudinal profiles tend not to exhibit marked changes across lithologic boundaries unless the slope becomes exceptionally steep. Although channel gradients over resistant lithologies are marginally steeper than those over weaker ones, the difference is often too subtle to be discerned either in numerical simulations or natural river profiles (Figs. 6, ??9, and 11). (Korup and Schlunegger, 2009) reported that the slope can vary by as much as 0.08 depending on lithology in hillslope areas. In comparison with their results, such abrupt lithology-driven slope changes do not occur in the alluvial-bedrock reaches investigated here.

This finding aligns with previous studies. Sklar and Dietrich (2006) demonstrated that the rock strength exerts only a limited influence on channel profiles in models that incorporate the sediment cover effect. Similarly, Guryan et al. (2024) showed that the variability in channel slope due to differences in rock erodibility is smoothed out when sediment cover dynamics are included in numerical simulations. The present study further supports these findings by demonstrating, through numerical experiments using field-derived datasets, that sediment cover effectively offsets the influence of bedrock strength on river profile morphology.

This study proposes that the relationship between the cover ratio and river slope is a critical factor, and the SFDM well reproduces this relationship. The ASPM does not consider the sediment cover ratio, and therefore, it fails to predict the actual river longitudinal profiles. While the SPACEM (Guryan et al., 2024) also considers the cover ratio, its reproducibility is inferior to that of the SFDM (Figs. **??** and **??**Fig. 9). The reason for this discrepancy lies in the formulation of the relationship between cover ratio P_c P_c and channel slope S in the SPACEM. Figure 12 (a), (b) illustrates cover ratio and erosional rates against slopes for both SPACEM and SFDM. Both models assume that the erosional rate is proportional to the ratio of bedrock exposure. In the case of SFDM, the bedrock exposure ratio is defined as $1-P_c$$1-P_\mathrm{c}$. In contrast, SPACEM adopts the log-scale definition e^{-H/H_*} , resulting in a weaker topographic response to variations in the ratio of sediment cover. At present, the former formulation is more suitable for representing actual river profiles. However, there is no physical basis to suggest that the cover ratio is linearly correlated with the sediment supply/transport capacity ratio; therefore, further investigation is necessary to improve the cover (or exposure) ratio to better fit real-world conditions in future research.

It is important to note that the present study focuses primarily on rivers that have approached a state of equilibrium between

It should be noted that several small-scale knickpoints are present in the rivers of the study area (Fig. 5) that cannot be explained by any of the models considered in this study. Most of these knickpoints occur independently of bedrock strength, and some display trends opposite to those expected from bedrock strength, such as occurring in relatively hard rock reaches with gentle channel gradients (Fig. 4). All models used in this study assume that rivers are in a steady-state balance between rock uplift and erosion. In contrast, rivers that are far from equilibriumconditions often exhibit distinctly steep channel gradients, characterized by prominent knickpoints propagating upstream. Around such knickpoints, sediment cover typically becomes minimal or absent, drastically reducing the buffering effect of sediment cover on rock erosion. Consequently, under disequilibrium conditions, differences in rock erodibility can more directly impact the shape of river longitudinal profilesThe presence of these minor knickpoints therefore suggests that parts of the river profiles may locally deviate from equilibrium. Knickpoints generated by the processes, such as past sea-level fluctuations or localized fault activity in bedrock rivers, are known to migrate upstream over time and eventually dissipate in upstream reaches (Whipple and Tucker, 1999). Such transient processes are not represented in equilibrium-based models. Despite these limitations, the models employed here—particularly the SFDM—successfully reproduce the overall longitudinal profile characteristics of the rivers. This indicates that, at a macroscopic scale, the river systems in the study area can reasonably be regarded as being close to equilibrium.

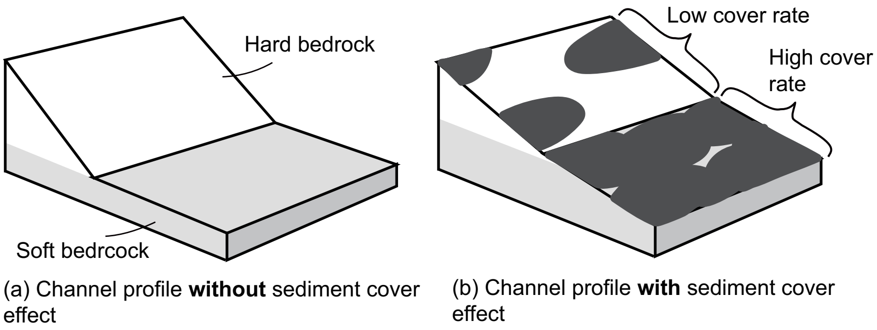

(a) Channel profile **without** sediment cover effect

(b) Channel profile **with** sediment cover effect

Figure 11. Comparison of channel profiles across two lithologies with and without sediment cover. (a) Without sediment cover. (b) With sediment cover.

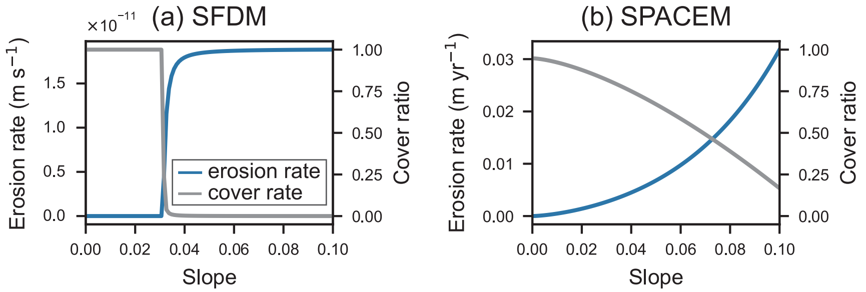

Figure 12. Changes in erosion rate and sediment cover ratio with slope in SFDM and SPACEM. The blue line represents changes in erosion rate, while the gray line indicates changes in sediment cover ratio. (a) SFDM result. Erosion rate and cover ratio change rapidly in a specific region of the slope. (b) SPACEM result. Both erosion rate and cover ratio change gently.

6.2 Lithologic Indirect lithologic controls for river longitudinal profiles

Although bedrock strength may not directly control local channel gradients, lithology can still exert an indirect influence on the entire morphology of channel longitudinal profiles by shaping the grain size distribution and sediment flux as mentioned in Lai et al. (2021). As shown in Eq. (21), the primary factors determining channel profiles are the water discharge per unit width q_w q_{w}, grain size D_s D_{s}, and sediment flux q_s q_{s}. Among these, the latter two parameters are potentially regulated by the lithologic characteristics of the upstream drainage areas.

Grain size and distributions of sediment are known to vary significantly depending on the lithology of their drainage basins (Kodama, 1994; Sklar et al., 2017; Roda-Boluda et al., 2018; Verdian et al., 2021; Takahashi, 2025)(Parker, 1991; Kodama, 1994; Sklar et al., 2017; Roda-Boluda et al., 2018; Verdian et al., 2021; Takahashi, 2025). Sediment grains are initially produced on hillslopes through physical and chemical weathering processes, where lithology, along with tectonics and climate, plays a critical role in determining grain sizes (Sklar, 2024). Field measurements have consistently highlighted the importance of lithology, owing to its control on the physical and chemical properties of parent rocks, in influencing grain size distribution. For instance, (Sklar et al.,

2017) Sklar et al. (2017) demonstrated a clear correlation between rock strength and the sizes of rock fragments measured in soils in California. Similarly, (Verdian et al., 2021) Verdian et al. (2021) conducted field measurements of clast sizes, indicating that gravels derived from massive granitic plutons exhibited the largest, those from surficial basalt flows had intermediate sizes, and those from marine ribbon chert were the smallest. Since tool size undergoes downstream fining through abrasion, local bedrock lithology alone does not uniquely determine channel gradient. In contrast, basin-integrated lithologic controls can still shape longitudinal profiles through their influence on tool production and size distributions. Collectively, these studies underscore the significant control exerted by hillslope lithology on grain size.

Bedrock lithology in hillslope regions also controls the ratio of bedloads to the eroded materials (Chatanantavet and Parker, 2009), which affects the sediment flux q_s q_s provided to streams. The sediment supply rate depends on the erosional rate, the drainage area, and the mode of mechanical weathering that determines the ratio of bedload materials in sediment (Eq. (17)). For example, (Roda-Boluda et al., 2018) Roda-Boluda et al. (2018) examined the frequency and size of landslides in southern Italy, focusing on their relationship with the local slope steepness and rock strength. They discovered that the frequency of landslides increases as the slope is composed of softer rock, which promotes the larger sediment production rates.

Thus, the lithologic composition of bedrock across the drainage basin from hill slopes hillslopes to fluvial zones can play a critical role in determining the overall longitudinal profile of river channels. Supporting this notion, the field-based analysis by Takahashi (2025) in the Tsugaru region of Japan demonstrated that variations in channel morphology are strongly linked to differences in sediment load and grain size, both of which are influenced by upstream lithology. The findings of this study are consistent with this interpretation. The bedrock types in the hillslope regions of the studied tributaries can be broadly divided into two categories: granodiorites and sedimentary rocks. Granodioritic bedrocks are predominantly exposed in the upstream catchments of Fukazawa and Sangasawa, whereas sedimentary rocks dominate the upstream areas of Takinosawa, Hisawa, and Gohyku Gohyaku River (Kubo et al., 2003; Yamamoto and Sakaguchi, 2023). Chi-plots analysis (Fig. 5) revealed that the channel steepness indices of Fukazawa and Sangasawa tended to be notably higher in their upper reaches compared to the other tributaries.

This pattern suggests that upstream lithology— specificallylithology—specifically, the presence of more resistant granodiorite—may enhance channel steepness by influencing sediment grain size and transport rates. These observations underscore the indirect yet significant role of lithologic variation in controlling longitudinal channel profile. Further quantitative predictions of such lithologic controls remain a key challenge for future research.

7 Conclusion

To investigate the influence of bedrock strength on fluvial morphology, this study combined field surveys with numerical experiments. The results revealed that the sediment cover effect plays a key role in mitigating the impact of variations in bedrock erodibility on river profile morphology.

Field surveys were conducted in the Abukuma River basin in northeastern Japan, where tributaries incise bedrock of varying lithologies exposed in close proximity. Bedrock strength and riverbed gravel grain size distributions were measured in each tributary. Tensile strength of bedrock samples, obtained through the Brazilian splitting test, varied by more than an order of magnitude. Despite this, no significant differences were observed in the channel slopes across the longitudinal profiles of these rivers (Fig. 6).

To explain the apparent insensitivity of river longitudinal profiles to local variations in bedrock strength, we carried out numerical experiments using three models that account for bedrock erodibility to different extents: the sediment-flux-dependent model (SFDM), the area-based stream power model (ASPM), and the stream power with alluvium conservation and entrainment model (SPACEM). All three incorporate bedrock erodibility, while SFDM and SPACEM also include the effects of sediment cover. Among them, only SFDM explicitly incorporates the sediment tool effect, which describes the enhanced erosion by mobile sediment particles.

The SFDM simulations demonstrated that the sediment cover effect buffers the influence of rock erodibility on channel slope. In regions with high bedrock erodibility, increased erosion tends to lower channel gradients. This reduction in slope, in turn, reduces sediment transport capacity, leading to greater sediment cover. The increased cover inhibits further erosion by reducing the sediment tool effect, establishing a negative feedback loop. This mechanism effectively dampens variations in slope, even in the presence of substantial differences in bedrock strength.

The numerical results emphasize the importance of incorporating both sediment cover and the sediment tool effect when evaluating the geomorphic consequences of bedrock erodibility. Among the three models, SFDM most accurately reproduced the observed longitudinal river profiles, exhibiting little to no slope variation in areas of differing lithology. In contrast, ASPM, which does not consider sediment cover, predicted prominent slope breaks inconsistent with field observations. SPACEM performed better by including sediment cover, but still exhibited unrealistic local slope variations, as it lacks explicit treatment of the sediment tool effect.

While bedrock strength does not directly control local channel gradients, this study suggests that upstream lithology can indirectly influence overall channel steepness by modifying sediment grain size and supply rates. Future research should aim to incorporate more extensive datasets on gravel characteristics to better quantify this indirect relationship between bedrock properties and fluvial morphology.

8 Notation

a	the ratio of the bedload to the total sediment supply.
A	drainage area (m^2).
A_0	a reference drainage area (m^2).
C_f	a friction coefficient.
D	a diameter of the specimen (m).
D_s D_{s}	grain diameter (m).
E	erosion rate ($\mathrm{m\ s^{-1}}$).
E_{eq} E_{eq}	erosion rate in steady state ($\mathrm{m\ s^{-1}}$).

E_r E_r	erosion rate in SPACEM (m yr^{-1}).
E_s E_s	rate of entraintment in SPACEM (m yr^{-1}).
g	acceleration of gravity (m s^{-2}).
H	thickness of sediment cover (m).
H_*	bedrock roughness scale (m).
I_r I_r	rate of particle impacts per unit area per unit time.
k k_SFDM	discharge coefficient in SFDM.
k_a k_SPACEM	discharge coefficient in SPACEM.
k_a	erosional coefficient (L^{1-2m} T^{-1}).
k_s k_s	hydraulic roughness height (m).
k_{sn} k_sn	normalized steepness.
k_v k_v	rock resistance coefficient.
k_w k_w	channel width coefficient.
K_r K_r	bedrock erodibility (L^{1-2m} T^{-1}).
$K_{\mathrm{r},i}$	the ith rock type erodibility.
K_{sed} K_sed	sediment erodibility.
L	length of the specimen (m).
L_E L_E	relative lithological erodibility index.
L_s L_s	saltation hop length (m).
m	a drainage area exponent in stream power models.
M_p M_p	particle mass (kg).
n	a slope exponent in stream power models.
$\bar{P}$	average precipitation rate (m^2 s^{-1}).
P_c $\bar{P}_\mathrm{yr}$	mean annual precipitation rate (m^2 yr^{-1}).
P_c	cover ratio.
P_{max} P_max	maximum load (kN).
q	water discharge per unit width (m^2 s^{-1}).
q_s q_s	sediment flux volume per unit width (m^2 s^{-1}).
q_t q_t	sediment transport capacity per unit width (m^2 s^{-1}).
Q_w q_w	water discharge (m per unit width (m^2 s^{-1}).
$q_\mathrm{w,yr}$	mean annual water discharge per unit width (m^2 yr^{-1}).
Q_w	water discharge (m^3 s^{-1}).
R_b $Q_\mathrm{w,yr}$	mean annual water discharge (m^3 yr^{-1}).
r	a correlation coefficient.
R_b	nondimensional buoyant density of sediment.

S	channel slope.
U	uplift rate (m s^{-1}).
U_i	particle impacr velocity (m s^{-1}).
V_i	average volume eroded per particle impact.
w_{si}	vertical sediment velocity on impact (m s^{-1}).
W	channel width (m).
W_s W_s	settling velocity (m s^{-1}).
x	distance along the channel from upstream (m).
Y	Young's modulus (MPa).
α	saltation impact angle.
α_d α_d	change rate of the grain diameter.
β_0	an empirical erosional coefficient.
ε_v ε_v	unit volume detachment energy (J m^{-3}).
η	bedrock elevation (m).
θ	channel concavity index.
κ_a κ_a	roughness coefficient linear to the grain size (m).
κ_b κ_b	bedrock roughness (m).
ρ_s ρ_s	sediment density (kg m^{-3}).
ρ_w ρ_w	water density (kg m^{-3}).
σ_t σ_t	bedrock tensile strength (MPa).
$\sigma_{t,i}$ $\sigma_{\mathrm{t},i}$	tensile strengths of the ith rock type (MPa).
$\sigma_{\mathrm{t,tuff}}$	tensile strength of tuff (MPa).
τ_b τ_b	bed shear stress (Pa).
τ^*	nondimensional bed shear stress.
τ_c^* τ_c^*	nondimentional critical shear stress.
ϕ	sediment porocity.

Code and data availability. All data and code supporting this study are openly available on Zenodo. Bedrock strength dataset: available at Zenodo, DOI: 10.5281/zenodo.17017130. Grain size analysis dataset: available at Zenodo, DOI: 10.5281/zenodo.17017613. River incision model calculation code and outputs: available at Zenodo, DOI: 10.5281/zenodo.18206634. DEM data were obtained from the Geospatial Information Authority of Japan, which are available via their web portal.

Author contributions. N.Y. and H.N. designed research; N.Y. performed research; N.Y. analyzed data; and N.Y and H.N. wrote the paper.

Competing interests. The authors declare no competing interest.

Acknowledgements. This work was supported by JSPS KAKENHI Grant Number 23K22872 and Sediment Dynamics Research Consortium (sponsored by INPEX, JAPEX, and JOGMEC). The authors used ChatGPT and Grammarly to enhance the clarity and readability of the manuscript during its preparation.

References

Akiba, T., Sano, S., Yanase, T., Ohta, T., and Koyama, M.: Optuna: A Next-generation Hyperparameter Optimization Framework, https://arxiv.org/abs/1907.10902, 2019.

Aubert, G., Langlois, V. J., and Allemand, P.: Bedrock incision by bedload: insights from direct numerical simulations, Earth Surface Dynamics, 4, 327–342, https://doi.org/10.5194/esurf-4-327-2016, 2016.

Bao, T., Hashiba, K., and Fukui, K.: Effect of Water Saturation on the Brazilian Tension Test of Rocks, MATERIALS TRANSACTIONS, 62, 48–56, https://doi.org/10.2320/matertrans.M-M2020857, 2021.

Beer, A. R., Turowski, J. M., and Kirchner, J. W.: Spatial patterns of erosion in a bedrock gorge, Journal of Geophysical Research: Earth Surface, 122, 191–214, https://doi.org/https://doi.org/10.1002/2016JF003850, 2017.

Bitter, J. G. A.: A study of erosion phenomena part I, Wear, 6, 5–21, https://doi.org/https://doi.org/10.1016/0043-1648(63)90003-6, 1963.

Brocard, G. Y., Willenbring, J. K., Scatena, F. N., and Johnson, A. H.: Effects of a tectonically-triggered wave of incision on riverine exports and soil mineralogy in the Luquillo Mountains of Puerto Rico, Applied Geochemistry, 63, p. 586– 598, https://doi.org/10.1016/j.apgeochem.2015.04.001, 2015.

Campforts, B., Vanacker, V., Herman, F., Vanmaercke, M., Schwanghart, W., Tenorio, G. E., Willems, P., and Govers, G.: Parameterization of river incision models requires accounting for environmental heterogeneity: insights from the tropical Andes, Earth Surface Dynamics, 8, 447–470, https://doi.org/10.5194/esurf-8-447-2020, 2020.

Carr, J., DiBiase, R., Yeh, E., Fisher, D., and Kirby, E.: Rock properties and sediment caliber govern bedrock river morphology across the Taiwan Central Range, Science Advances, 9, https://doi.org/10.1126/sciadv.adg6794, publisher Copyright: Copyright © 2023 The Authors, some rights reserved;, 2023.

Chatanantavet, P. and Parker, G.: Physically based modeling of bedrock incision by abrasion, plucking, and macroabrasion, Journal of Geophysical Research Atmospheres, 114, https://doi.org/10.1029/2008JF001044, 2009.

Conrad, O., B. B. B. M. D. H. F. E. G. L. W. J. W. V. and Böhner, J.: System for Automated Geoscientific Analyses (SAGA) v. 2.1.4, 8, https://doi.org/10.5194/gmd-8-1991-2015, 2015.

Cruz Nunes, F., Delunel, R., Schlunegger, F., Akçar, N., and Kubik, P. W.: Bedrock bedding, landsliding and erosional budgets in the Central European Alps, Terra Nova, 27, 370–378, https://doi.org/https://doi.org/10.1111/ter.12169, 2015.

E. Meyer-Peter, R. M.: Formulas for Bed-Load transport, pp. 39–64, https://repository.tudelft.nl/islandora/object/uuid%3A4fda9b61-be28-4703-ab06-43cdc2a21bd7/datastream/OBJ/download, 1948.

Engle, P. A.: Impact Wear of Materials, Elsevier Sci., New York, 1978.

Fernández, R., Parker, G., and Stark, C. P.: Experiments on patterns of alluvial cover and bedrock erosion in a meandering channel, Earth Surface Dynamics, 7, 949–968, https://doi.org/10.5194/esurf-7-949-2019, 2019.

Finnegan, N. J., Roe, G., Montgomery, D. R., and Hallet, B.: Controls on the channel width of rivers: Implications for modeling fluvial incision of bedrock, Geology, 33, 229–232, https://doi.org/10.1130/G21171.1, 2005.

Fujiwara, O., Yanagida, M., and Sanga, T.: Late Pleistocene to Holocene Vertical Displacement Rates in Japanese Islands, The Earth Monthly, 26, 442–447, 2004.

Fujiwara, O., Makoto, Y., Sanga, T., and Moriya, T.: Researches on tectonic uplift and denudation with relation to geological disposal of HLW in Japan, Nuclear Fuel Cycle and Environment, 11, 113–124, https://doi.org/10.3327/jnuce.11.113, 2005.

Fukuda, S., Sueoka, S., Kohn, B. P., and Tagami, T.: (U–Th)/He thermochronometric mapping across the Northeast Japan Arc: towards understanding mountain building in an island-arc setting, Earth, Planets and Space, 72, https://doi.org/https://doi.org/10.1186/s40623-020-01151-z, 2020.

Gilbert, G. K.: Report on the geology of the Henry Mountains, U.S. Government Printing Office, https://doi.org/https://doi.org/10.3133/70039916, 1877.

Goren, L. and Shelef, E.: Channel concavity controls planform complexity of branching drainage networks, Earth Surface Dynamics, 12, 1347–1369, https://doi.org/10.5194/esurf-12-1347-2024, 2024.

Guryan, G. J., Johnson, J. P. L., and Gasparini, N. M.: Sediment Cover Modulates Landscape Erosion Patterns and Channel Steepness in Layered Rocks: Insights From the SPACE Model, Journal of Geophysical Research: Earth Surface, 129, e2023JF007 509, https://doi.org/https://doi.org/10.1029/2023JF007509, e2023JF007509 2023JF007509, 2024.

Haag, M. B., Schoenbohm, L. M., Wolpert, J., Jess, S., Bierman, P., Corbett, L., Sommer, C. A., and Endrizzi, G.: Rock strength controls erosion in tectonically dead landscapes, Science Advances, 11, eadr2610, https://doi.org/10.1126/sciadv.adr2610, 2025.

Hayakawa, Y. S. and Oguchi, T.: GIS analysis of fluvial knickzone distribution in Japanese mountain watersheds, Geomorphology, 111, 27–37, https://doi.org/https://doi.org/10.1016/j.geomorph.2007.11.016, gIS and SDA applications in geomorphology, 2009.

Howard, A. D.: A detachment-limited model of drainage basin evolution, Water Resources Research, 30, 2261–2285, https://doi.org/https://doi.org/10.1029/94WR00757, 1994.

Howard, A. D. and Kerby, G.: Channel changes in badlands, GSA Bulletin, 94, 739–752, https://doi.org/10.1130/0016-7606(1983)94<739:CCIB>2.0.CO;2, 1983.

Ichikawa, K.: Pre-Cretaceous terranes of Japan, publication of IGCP Project No. 224, Pre-Jurassic evolution of Eastern Asia, 1990.

Inoue, T., Izumi, N., Shimizu, Y., and Parker, G.: Interaction among alluvial cover, bed roughness, and incision rate in purely bedrock and alluvial-bedrock channel, Journal of Geophysical Research: Earth Surface, 119, 2123–2146, https://doi.org/https://doi.org/10.1002/2014JF003133, 2014.

Inoue, T., Yamaguchi, S., and Nelson, J. M.: The effect of wet-dry weathering on the rate of bedrock river channel erosion by saltating gravel, Geomorphology, 285, 152–161, https://doi.org/https://doi.org/10.1016/j.geomorph.2017.02.018, 2017.

Johnson, J., Whipple, K., Sklar, L., and Hanks, T.: Transport slopes, sediment cover, and bedrock channel incision in the Henry Mountains, Utah, J. Geophys. Res, 114, https://doi.org/10.1029/2007JF000862, 2009.

Kühni, A. and Pfiffner, O.: The relief of the Swiss Alps and adjacent areas and its relation to lithology and structure: topographic analysis from a 250-m DEM, Geomorphology, 41, 285–307, https://doi.org/https://doi.org/10.1016/S0169-555X(01)00060-5, 2001.

Kodama, Y.: Downstream changes in the lithology and grain size of fluvial gravels, the Watarase River, Japan; evidence of the role of abrasion in downstream fining, Journal of Sedimentary Research, 64, 68–75, https://doi.org/10.1306/D4267D0C-2B26-11D7-8648000102C1865D, 1994.

Korup, O. and Schlunegger, F.: Rock-type control on erosion-induced uplift, eastern Swiss Alps, Earth and Planetary Science Letters, 278, 278–285, https://doi.org/https://doi.org/10.1016/j.epsl.2008.12.012, 2009.

Kubo, K., Yanagisawa, Y., Yamamoto, T., Komazawa, M., Hiroshima, T., and Sudou, S.: Geological Map, 1:200,000, Fukushima, Tech. Rep. NJ-54-16,22, Geological survey of Japan, AIST, 2003.

Lai, L. S.-H., Roering, J. J., Finnegan, N. J., Dorsey, R. J., and Yen, J.-Y.: Coarse sediment supply sets the slope of bedrock channels in rapidly uplifting terrain: Field and topographic evidence from eastern Taiwan, Earth Surface Processes and Landforms, 46, 2671–2689, https://doi.org/https://doi.org/10.1002/esp.5200, 2021.

Lamb, M., Dietrich, W., and Sklar, L.: A model for fluvial bedrock incision by impacting suspended and bed load sediment, J. Geophys. Res., 113, https://doi.org/10.1029/2007JF000915, 2008.

Luque, R. F. and and, R. V. B.: Erosion And Transport Of Bed-Load Sediment, Journal of Hydraulic Research, 14, 127–144, https://doi.org/10.1080/00221687609499677, 1976.

Mair, D., Witz, G., Do Prado, A. H., Garefalakis, P., and Schlunegger, F.: Automated detecting, segmenting and measuring of grains in images of fluvial sediments: The potential for large and precise data from specialist deep learning models and transfer learning, Earth Surface Processes and Landforms, 49, 1099–1116, https://doi.org/https://doi.org/10.1002/esp.5755, 2024.

Matsushi, Y., Matsuzaki, H., and Makino, H.: Testing Models of Landform Evolution by Determining the Denudation Rates of Mountainous Watersheds using Terrestrial Cosmogenic Nuclides, Japanese Geomorphological Union, 35, 165–185, https://cir.nii.ac.jp/crid/1520290882637797888, 2014.

Miller, K. L., Szabó, T., Jerolmack, D. J., and Domokos, G.: Quantifying the significance of abrasion and selective transport for downstream fluvial grain size evolution, Journal of Geophysical Research: Earth Surface, 119, 2412–2429, https://doi.org/https://doi.org/10.1002/2014JF003156, 2014.

Molnar, P.: Climate change, flooding in arid environments, and erosion rates, Geology, 29, 1071–1074, https://doi.org/10.1130/0091-7613(2001)029<1071:CCFIAE>2.0.CO;2, 2001.

Molnar, P. and England, P.: Late Cenozoic uplift of mountain ranges and global climate change: chicken or egg?, 346, 29–34, https://doi.org/https://doi.org/10.1038/346029a0, 1990.

O'Callaghan, J. F. and Mark, D. M.: The extraction of drainage networks from digital elevation data, Computer Vision, Graphics, and Image Processing, 28, 323–344, https://doi.org/https://doi.org/10.1016/S0734-189X(84)80011-0, 1984.

Parker, G.: Selective sorting and abrasion of river gravel. I: Theory, Journal of Hydraulic Engineering, 117, 131–147, https://doi.org/10.1061/(ASCE)0733-9429(1991)117:2(131), 1991.

Perron, J. T. and Royden, L.: An integral approach to bedrock river profile analysis, Earth Surface Processes and Landforms, 38, 570–576, https://doi.org/https://doi.org/10.1002/esp.3302, 2013.

Pritchard, D., Roberts, G., White, N., and Richardson, C.: Uplift histories from river profiles, Geophysical Research Letters, 36, https://doi.org/10.1029/2009GL040928, 2009.

Roberts, G. G., White, N. J., Martin-Brandis, G. L., and Crosby, A. G.: An uplift history of the Colorado Plateau and its surroundings from inverse modeling of longitudinal river profiles, Tectonics, 31, https://doi.org/https://doi.org/10.1029/2012TC003107, 2012.

Roda-Boluda, D. C., D'Arcy, M., McDonald, J., and Whittaker, A. C.: Lithological controls on hillslope sediment supply: insights from landslide activity and grain size distributions, Earth Surface Processes and Landforms, 43, 956–977, https://doi.org/https://doi.org/10.1002/esp.4281, 2018.

Seidl, M. A. and Dietrich, W. E.: The problem of channel erosion into bedrock, Catena Suppl., 23, 101–124, 1992.

Shobe, C. M., Tucker, G. E., and Barnhart, K. R.: The SPACE 1.0 model: a Landlab component for 2-D calculation of sediment transport, bedrock erosion, and landscape evolution, Geoscientific Model Development, 10, 4577–4604, https://doi.org/10.5194/gmd-10-4577-2017, 2017.

Sklar, L. and Dietrich, W. E.: River Longitudinal Profiles and Bedrock Incision Models: Stream Power and the Influence of Sediment Supply, pp. 237–260, American Geophysical Union (AGU), ISBN 9781118664292, https://doi.org/https://doi.org/10.1029/GM107p0237, 1998.

Sklar, L. S.: Grain Size in Landscapes, Annual Review of Earth and Planetary Sciences, 52, 663–692, https://doi.org/https://doi.org/10.1146/annurev-earth-052623-075856, 2024.

Sklar, L. S. and Dietrich, W. E.: Sediment and rock strength controls on river incision into bedrock, Geology, 29, 1087–1090, https://doi.org/10.1130/0091-7613(2001)029<1087:SARSCO>2.0.CO;2, 2001.

Sklar, L. S. and Dietrich, W. E.: A mechanistic model for river incision into bedrock by saltating bed load, Water Resources Research, 40, https://doi.org/https://doi.org/10.1029/2003WR002496, 2004.

Sklar, L. S. and Dietrich, W. E.: The role of sediment in controlling steady-state bedrock channel slope: Implications of the saltation abrasion incision model, Geomorphology, 82, 58–83, https://doi.org/10.1016/j.geomorph.2005.08.019, 2006.

Sklar, L. S., Riebe, C. S., Marshall, J. A., Genetti, J., Leclere, S., Lukens, C. L., and Merces, V.: The problem of predicting the size distribution of sediment supplied by hillslopes to rivers, Geomorphology, 277, 31–49, https://doi.org/https://doi.org/10.1016/j.geomorph.2016.05.005, connectivity in Geomorphology from Binghamton 2016, 2017.

Snelder, T. H., Lamouroux, N., and Pella, H.: Empirical modelling of large scale patterns in river bed surface grain size, Geomorphology, 127, 189–197, https://doi.org/https://doi.org/10.1016/j.geomorph.2010.12.015, 2011.

Society, T. J. G.: Japanese Geotechnical Society standards : laboratory testing standards of geomaterials, Japan Geotechnical Society and Maruzen Publishing [distributor], https://cir.nii.ac.jp/crid/1130848328362029184, 2016.

Soloy, A., Turki, I., Fournier, M., Costa, S., Peuziat, B., and Lecoq, N.: A Deep Learning-Based Method for Quantifying and Mapping the Grain Size on Pebble Beaches, Remote Sensing, 12, https://doi.org/10.3390/rs12213659, 2020.

Steer, P., Guerit, L., Lague, D., Crave, A., and Gourdon, A.: Size, shape and orientation matter: fast and semi-automatic measurement of grain geometries from 3D point clouds, Earth Surface Dynamics, 10, 1211–1232, https://doi.org/10.5194/esurf-10-1211-2022, 2022.

Sternberg, H.: Untersuchungen über längen-und Querprofil geschiebeführende Flüsse, Zeitschrift für Bauwesen, 25, 483–506, https://cir.nii.ac.jp/crid/1572824500838774016, 1875.

Takahashi, N. O.: Relative role of rock erodibility and sediment load in setting channel slope of mountain rivers, Earth Surface Processes and Landforms, 50, e70 017, https://doi.org/https://doi.org/10.1002/esp.70017, 2025.

Takayama, S.: Study on Bedload Gravels in Mountain Streams near Kaifuura, Niigata Prefecture (Part II), Geological Review of Japan, 38, 415–425, https://doi.org/10.4157/grj.38.415, 1965.

Tanaka, K., Toda, S., Ueda, K., and Chigira, M.: Long-term characteristics of geological conditions in Japan (Part 2) proposal and application the method for evaluation of uplift-subsidence., Denryoku chuo kenkyujyo hokoku, U96028, 809–826, 1996.

Tucker, G. and Slingerland, R.: Erosional dynamics, flexural isostasy, and long-lived escarpments: A numerical modeling study, Journal of Geophysical Research, 99, https://doi.org/10.1029/94JB00320, 1994.

Tucker, G. and Whipple, K.: Topographic outcomes predicted by stream erosion models: Sensitivity analysis and intermodel comparison, Journal of Geophysical Research, 107, 2179, https://doi.org/10.1029/2001JB000162, 2002.

Turowski, J. M., Lague, D., and Hovius, N.: Cover effect in bedrock abrasion: A new derivation and its implications for the modeling of bedrock channel morphology, Journal of Geophysical Research: Earth Surface, 112, https://doi.org/https://doi.org/10.1029/2006JF000697, 2007.

Turowski, J. M., Pruß, G., Voigtländer, A., Ludwig, A., Landgraf, A., Kober, F., and Bonnelye, A.: Geotechnical controls on erodibility in fluvial impact erosion, Earth Surface Dynamics, 11, 979–994, https://doi.org/10.5194/esurf-11-979-2023, 2023.

Verdian, J. P., Sklar, L. S., Riebe, C. S., and Moore, J. R.: Sediment size on talus slopes correlates with fracture spacing on bedrock cliffs: implications for predicting initial sediment size distributions on hillslopes, Earth Surface Dynamics, 9, 1073–1090, https://doi.org/10.5194/esurf-9-1073-2021, 2021.

Vutukuri, V., Lama, R., and Saluja, S.: Handbook on mechanical properties of rocks. Volume 1: Testing techniques and results, Trans Tech Publishers, 1974.

Whipple, K., DiBiase, R., and Crosby, B.: 9.28 Bedrock Rivers, vol. 9, pp. 550–573, ISBN 9780080885223, https://doi.org/10.1016/B978-0-12-374739-6.00254-2, 2013.

Whipple, K. X.: Bedrock rivers and the geomorphology of active orogens, Annual Review of Earth and Planetary Sciences, 32, 151–185, https://doi.org/10.1146/annurev.earth.32.101802.120356, 2004.

Whipple, K. X. and Tucker, G. E.: Dynamics of the stream-power river incision model: Implications for height limits of mountain ranges, landscape response timescales, and research needs, Journal of Geophysical Research: Solid Earth, 104, 17 661–17 674, https://doi.org/https://doi.org/10.1029/1999JB900120, 1999.

Whipple, K. X. and Tucker, G. E.: Implications of sediment-flux-dependent river incision models for landscape evolution, Journal of Geophysical Research: Solid Earth, 107, ETG 3–1–ETG 3–20, https://doi.org/https://doi.org/10.1029/2000JB000044, 2002.

Wobus, C., Whipple, K. X., Kirby, E., Snyder, N., Johnson, J., Spyropolou, K., Crosby, B., and Sheehan, D.: Tectonics from topography: Procedures, promise, and pitfalls, in: Tectonics, Climate, and Landscape Evolution, Geological Society of America, ISBN 9780813723983, https://doi.org/10.1130/2006.2398(04), 2006.

Yamamoto, T. and Sakaguchi, K.: Geology of the Bandai San District, Tech. Rep. 32, Geological survey of Japan, AIST, 2023.

Yoshiyama, A. and Yanagida, M.: Uplift Rates Estimated from Relative Heights of Fluvial Terrace Surfaces and Valley Bottoms, Jornal of Geography, 104, 809–826, https://doi.org/10.5026/jgeography.104.6_809, 1995.